CHEMISTRY OF MATERIALS

pubs.acs.org/cm

Article

Linker-Dependent Stability of Metal-Hydroxide Organic Frameworks for Oxygen Evolution

Daniel J. Zheng,[▽] Mikaela Görlin,[▽] Kaylee McCormack, Junghwa Kim, Jiayu Peng, Hongbin Xu, Xiaoxin Ma, James M. LeBeau, Roland A. Fischer, Yuriy Román-Leshkov,* and Yang Shao-Horn*

Cite This: https://doi.org/10.1021/acs.chemmater.3c00316

Read Online

ACCESS | Metrics & More | Article Recommendations | Supporting Information

ABSTRACT: Metal−organic frameworks (MOFs) are periodic organic−inorganic materials that have garnered considerable attention for electrocatalytic applications due to their wide tunability. Metal-hydroxide organic frameworks (MHOFs), a subset of MOFs that combine layered metal hydroxides with organic ligands of various $\pi-\pi$ stacking energy, have shown promising catalytic functions, such as for the oxygen evolution reaction (OER). The long-term electrochemical stability of these materials for the OER is unfortunately not well understood, which is critical to design practical devices. In this study, we investigated how Ni-based MHOFs composed of two linkers with different $\pi-\pi$ interaction strength (terephthalate; L1 and azobenzene-4,4′-dicarboxylate; L4) change as a function of cycle number and potential for the OER. All MHOFs tested showed significant increases in the number of electrochemically active Ni sites and OER activity when cycled. MHOFs constructed using the linkers with stronger $\pi-\pi$ stacking energy (L4) were observed to remain intact in bulk with only near-surface transformations to $NiOOH_{2-x}$-like phases, whereas MHOFs with linkers of weaker $\pi-\pi$ stacking energy (L1) showed complete reconstruction to $NiOOH_{2-x}$-like phases. This was confirmed using X-ray diffraction, X-ray absorption spectroscopy, and electron microscopy. Further, in situ characterization using Raman and UV−vis revealed that the presence of stable linkers within the MHOF structure suppresses the $Ni^{2+}/Ni^{(3+\delta)+}$ redox process. We further identify $NiOOH_{2-x}$ as the OER active phase, while the MHOF phase serves as a precatalyst. We further propose a detailed mechanism for the phase transformation, which provides valuable insights into the future challenges for the design of both stable and catalytically active MOF-based materials for water oxidation.

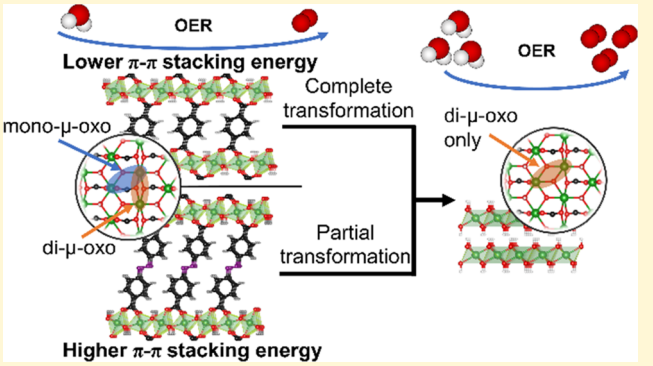

INTRODUCTION

The oxygen evolution reaction (OER) is essential for the production of renewable fuels and chemicals, such as hydrogen production from electrochemical water splitting, value-added hydrocarbons from CO_2 electro-reduction, and ammonia electro-synthesis from nitrogen.[1] However, the sluggish kinetics of OER, even when catalyzed by precious-metal oxide catalysts,[2] still limit the efficiency of such devices.[3] In order to decrease the cost and increase the feasibility of these devices at scale for practical applications,[4] it is critical to develop sustainable and highly active OER catalysts. The most active OER electrocatalysts are still at least an order of magnitude less active on a per active site basis than that of oxygen-evolving complexes found in biological systems that intricately combine metal-oxo clusters with organic ligands to give unrivaled OER activity.[5] In efforts to mimic the superiority of biological systems for electrochemical water oxidation, there has been considerable effort in engineering metal−organic frameworks (MOFs) as OER electrocatalysts due to their supramolecular chemistry that connects inorganic metal or metal oxide clusters using organic ligands in a crystalline and reticular fashion.[6,7]

MOFs and MOF-derived catalysts have been studied for many electrochemical reactions,[8] including hydrogen evolution,[9] oxygen reduction,[10,11] and oxygen evolution reaction.[12−14] Unfortunately, MOFs can be unstable during electrochemical reactions such as the OER and may convert to (oxy)hydroxides.[15−17] For example, Zhao et al. demonstrated the structural transformations of $Ni_{0.5}Co_{0.5}$-MOF-74 to $Ni_{0.5}Co_{0.5}OOH$ during OER using operando X-ray absorption spectroscopy (XAS).[18] Recently, Yuan et al. have designed metal-hydroxide organic frameworks (MHOFs) that are composed of edge-sharing metal-hydroxide octahedral sheets

Received: February 16, 2023
Revised: June 7, 2023

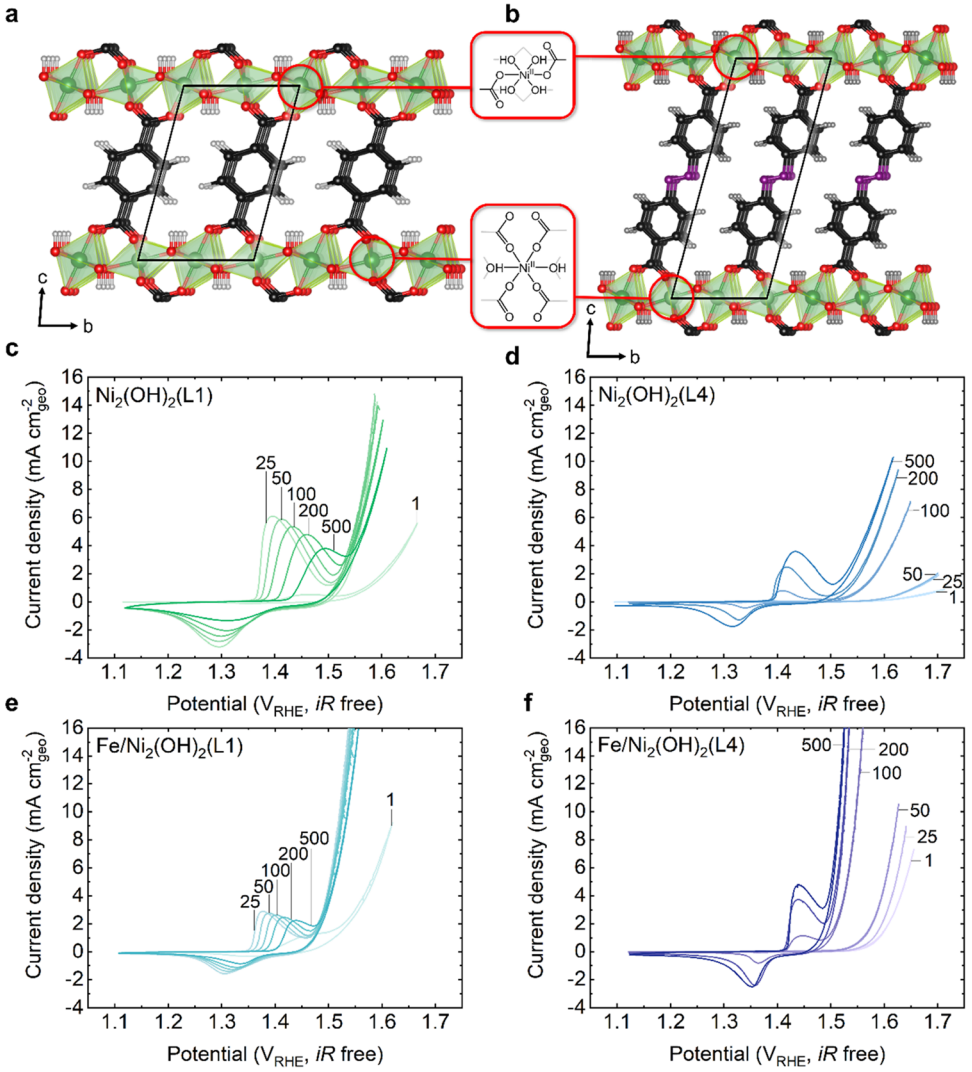

Figure 1. Structure of (a) $Ni_2(OH)_2$(L1) and (b) $Ni_2(OH)_2$(L4) metal-hydroxide organic frameworks viewed normal to the *a* direction. L1, terephthalate; L4, azobenzene-4,4′-dicarboxylate. The insets highlight the two crystallographically unique Ni coordination environments within the structure. Color scheme: Ni, green; O, red; C, brown; N, purple; H; gray. The black boxes designate a single unit cell of the material. OER polarization curves of (c) $Ni_2(OH)_2$(L1), (d) $Ni_2(OH)_2$(L4), (e) $Fe/Ni_2(OH)_2$(L1), and (f) $Fe/Ni_2(OH)_2$(L4) metal-hydroxide organic frameworks cycled between 1.1 and 1.7 V_{RHE} for 500 cycles at 1600 rpm and at a scan rate of 10 mV s^{-1} in O_2-saturated 0.1 M KOH. Electrodes were composed of 125 μg_{MHOF} $cm_{geo.}^{-2}$ and 14 μg_{Nafion} $cm_{geo.}^{-2}$ on 0.196 cm^2 glassy carbon disk.

cross-linked with organic linkers, which show tunable metal redox potential and electrochemical OER activity via metal substitution.[19] While the leaching of organic linkers from MHOFs in 0.1 M KOH can be reduced significantly with greater $\pi-\pi$ stacking energy of the linkers,[19] the long-term structural stability of these materials during the OER requires further investigation.[20] Therefore, it is imperative to gain an in-depth understanding of how such MHOFs change during electrochemical reactions in order to rationally design stable organic−inorganic hybrid materials with active sites resembling those of molecular or biological catalysts.

Here, we investigate the stability of MHOF nanosheets with two different linkers—terephalate (L1) and azobenzene-4,4′-dicarboxylate (L4)—during the OER in 0.1 M KOH. The L1 and L4 linkers were chosen for this study as they exhibit a large disparity in $\pi-\pi$ interaction energies and MHOFs incorporating them previously exhibited the largest difference in chemical stability in alkaline solutions.[19] Upon cyclic voltammetry between 1.1 and 1.7 V vs the reversible hydrogen electrode (V_{RHE}), both the fraction of electrochemically active metal sites and the OER activity of these MHOFs increase with increasing cycle number. The MHOF nanosheets with the L1 linker show complete bulk decomposition to (oxy)hydroxide-like phases (denoted as "$NiOOH_{2-x}$", where x is the electrons, and hence the protons, lost from the Ni^{2+} ground state structure), while the L4 analogues show only transformation of near-surface regions according to X-ray diffraction (XRD), scanning transmission electron microscopy (STEM), and X-ray absorption spectroscopy (XAS) measurements. We further utilized in situ surface-enhanced Raman and UV−vis spectroscopies of the MHOF nanosheets during the OER to unveil the relationship between linker loss, number electrochemically active Ni sites, and transformation of MHOF to $NiOOH_{2-x}$-like phases. We conclude by proposing possible transformation pathways from the MHOF to $NiOOH_{2-x}$-like structures via loss of organic linkers, which happens spontaneously, but is also facilitated by the oxidation of Ni^{2+} to $Ni^{(3+\delta)+}$.

https://doi.org/10.1021/acs.chemmater.3c00316
Chem. Mater. XXXX, XXX, XXX−XXX

EXPERIMENTAL METHODS

Synthesis of Metal-Hydroxide Organic Framework Nanosheets. We selected Ni MHOFs with and without Fe substitution along with having two different ligands, the L1 linker in Figure 1a or L4 linker in Figure 1b, to understand the stability of MHOFs during electrochemical water oxidation. Four different compositions of MHOF nanosheets were synthesized through solvothermal methods reported previously,[19] which are referred to as $Ni_2(OH)_2$(L1), Fe/$Ni_2(OH)_2$(L1), $Ni_2(OH)_2$(L4), and Fe/$Ni_2(OH)_2$(L4). Detailed synthesis conditions can be found in the Supporting Information. Ni- and Fe-substituted MHOFs were studied as their (oxy)hydroxide analogues show the lowest overpotential for OER in alkaline environments and currently have the most commercial interest,[21,22] making them serve as prime model systems to study the response of MHOFs under OER conditions. As previous work showed that Ni MHOFs with ∼12.5 atom % Fe substitution had the highest OER activity,[19] we aimed to study MHOFs with a similar level of Fe substitution, which was confirmed to be ∼15 at% using inductively coupled plasma-mass spectrometry (ICP-MS) in Table S1.

Electrochemical Characterization. Electrodes were prepared by drop-casting a prepared ink of the MHOFs on a circular 5 mm diameter glassy carbon (GC) disk electrode (Pine Research) with a nominal loading of 125 μg_{MHOFs} $cm_{geo.}^{-2}$ and 14 μg_{Nafion} cm_{geo}^{-2}. See the Supporting Information for a detailed electrode and ink preparation procedure. Some investigations were also conducted of MHOFs loaded on carbon as support, which was prepared by adding 1 mg of acid-treated acetylene black during the ink preparation, giving an electrode loading of 25 μg_{carbon} $cm_{geo.}^{-2}$ or 20 wt % acetylene black carbon. For the XRD and XAS measurements that required a larger quantity of cycled materials for characterization, the prepared ink was deposited on 8 cm^2 porous carbon felt electrodes with a loading of 6.25 mg_{MHOF} $cm_{geo.}^{-2}$ and 0.7 mg_{Nafion} cm_{geo}^{-2}.

Rotating disk electrode (RDE) measurements were performed in a three-electrode setup in a glass or PTFE electrochemical cell using a Hg/HgO reference electrode (4.24 M KOH filling solution, Pine Research) and a Pt wire counter electrode in a rotating disk setup in O_2-saturated 0.1 M as-received KOH (semiconductor grade, 99.99% trace metals basis, Sigma-Aldrich). The 0.1 M KOH electrolyte was purified (see the Supporting Information for the procedure) for selected measurements using a protocol reported previously.[23] The potential was controlled using a Biologic VSP-300 potentiostat and the electrode rotation rate was controlled using a Pine Research Modulated Speed Rotator. Cyclic voltammetry (CV) with various potential cutoff ranges was conducted with a scan rate of 10 mV s^{-1} and 1600 rpm rotation speed. For carbon felt electrodes, a lower cutoff potential was used to minimize bubble formation from the higher OER currents due to the higher catalyst loading. The uncompensated solution resistance (R_u) was determined using electrochemical impedance spectroscopy (EIS) and subtracted from the measured potential at each current (i) to correct for the Ohmic (iR) drop. The materials were subsequently collected after electrochemical testing by ultrasonicating the GC disk in 0.5 mL ethanol for 30 min. Redox-derived turnover frequency (TOF_{redox}) calculations are described in Supporting Note 1.

Material Characterization. X-ray diffractograms were recorded on a Bruker Discover D8-Focus Bragg-Brentano X-ray powder diffractometer using a Cu source (λ = 1.5418 Å) at 40 kV and 40 mA. X-ray diffraction of the synthesized MHOFs revealed high crystallinity and is in good agreement with previous work (Figure S1).[19] Atomic-resolution scanning transmission electron microscopy (STEM) imaging was conducted using a probe-aberration corrected Thermo Fisher Scientific Themis Z G3 60−300 kV S/TEM at 200 kV. Annular dark-field (ADF), bright-field (BF), and integrated differential phase contrast (iDPC) STEM images were acquired with a convergence semiangle of 18.9 mrad. Further, STEM images were acquired using a total dose of less than ∼125 e^- /Å^2 to minimize the electron beam-induced structural degradation. Energy-dispersive X-ray spectroscopy (EDX) data were collected using a Thermo Fisher Scientific Super-X detector. Electron energy loss (EEL) spectra were collected using a Gatan Imaging Filter 1066HR using 0.3 eV/ch energy dispersion, which yielded a full width at half-maximum energy resolution of 1.5 eV.

X-ray photoelectron spectroscopy (XPS) was performed on a PHI Versaprobe II instrument equipped with a multiple-channel hemispherical analyzer and a monochromatic Al anode X-ray source operating at 100 W. Samples were mounted to the platen on insulating tape and measurements were performed when the pressure in the main chamber approached 10^{-9} Torr. A beam with a 200 μm spot size was scanned over the sample surface, while a dual-beam charge neutralization system was used with an argon ion beam energy of 10 eV. The XPS analysis procedure is detailed in the Supporting Information.

X-ray Absorption Spectroscopy. Ni K-edge XAS spectra were collected at the Stanford Synchrotron Radiation Lightsource (SSRL), Stanford Linear Accelerator Center (SLAC) at beamline 2−2 with a double-crystal Si (220) monochromator. XANES and EXAFS measurements were performed ex situ at room temperature in the transmission geometry (using nitrogen-filled ionized chambers) with pellet-pressed samples prepared with cellulose diluent sealed with X-ray transparent Kapton tape. The spectrum of Ni foil was recorded simultaneously and used for energy alignment. Spectra were collected at the Ni K-edge before and after electrochemical cycling of $Ni_2(OH)_2$(L4) and Fe/$Ni_2(OH)_2$(L4). Nine scans were averaged and merged with a spline up to k = 15.1 to improve the signal-to-noise ratio. Details of the analysis can be found in Supporting Note 2.

In Situ Surface-Enhanced Raman Spectroscopy. Surface-enhanced Raman spectroscopy (SERS) was carried out using a HORIBA microscope (see the Supporting Information for more information). The Au electrode was polished and electro-roughened to generate a SERS-active surface according to standard procedures (see also the Supporting Information).[24,25] The Au disk was fitted into rotating disk electrode holders (Pine) and inserted from the bottom of the electrochemical cell. A Pt wire was used as the counter electrode and a leak-free Ag/AgCl as the reference electrode (eDAQ), which were fitted through the side of the cell. All measurements were carried out in ∼1.5 mL purified 0.1 M KOH. The potential was stepped from 1.2 to 1.7 V_{RHE} and back to 1.2 V_{RHE} and spectra were collected after a steady-state current was measured. Since Raman probes mainly Raman-active modes with a high scattering cross section (such as phases with $Ni^{(3+\delta)+}$), it does not quantitatively account for underlying phases with a weaker cross section (such as reduced Ni^{2+}).[24,26]

In Situ UV−Vis Spectroelectrochemistry. UV−vis spectroelectrochemical measurements were carried out using a Genesys 180 spectrometer (ThermoScientific). Fluorine-doped-tin-oxide (FTO) substrates with a geometric area of ∼ 0.7 cm^2 (∼7 Ω sq^{-1}, Sigma-Aldrich) were used as working electrodes. The geometric loading of the MHOFs was ∼63 μg_{MHOF} cm_{geo}^{-2}. A strip of Cu tape was used as electrical contact and protected from the electrolyte with Kapton tape. Plastic UV−vis cuvettes with a transmission between 300 and 900 nm were employed as electrochemical cells, and the measurements were performed in 0.1 M KOH electrolyte used without further purifications. A leak-free Ag/AgCl electrode (eDAQ, Inc.) was used as the reference electrode and a Pt wire as the counter electrode. Spectra were recorded between 200 and 1000 nm with a resolution of 2 nm during steady-state conditions applying a fixed potential. The samples were aged by CV cycling between 1.2 and 1.7 V_{RHE} at 10 mV s^{-1} for 500 cycles. Potentiodynamic CV cycling was performed at 2 mV s^{-1} while monitoring the UV−vis absorbance at 550 nm. The measurements were performed without rotation and without purging the electrolyte to avoid disturbance of the UV−vis signal. The absolute OER activities may therefore differ from the RDE characterization. The UV−vis absorbance was converted to the molar extinction coefficient ($\varepsilon(\lambda)$) according to the Beer−Lambert law using the moles of Ni on the pristine electrodes determined using ICP-MS, following the procedure reported in earlier work.[27] However, this normalization does not account for losses of active material during the measurements.

https://doi.org/10.1021/acs.chemmater.3c00316
Chem. Mater. XXXX, XXX, XXX−XXX

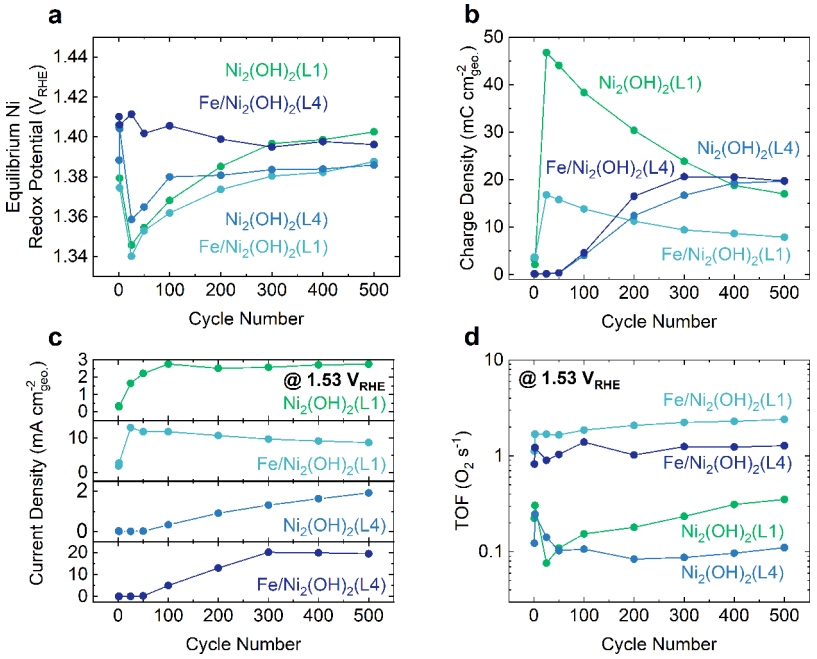

Figure 2. Electrochemical measurements of MHOF nanosheet as a function of cycle number during OER from 1.1 to 1.7 V_{RHE} in O_2-saturated 0.1 M KOH. (a) Equilibrium Ni redox peak potential (defined as the average between the peak potential at maximum peak current of the oxidation and the reduction peaks), (b) the charge density of the pre-OER $Ni^{2+}/Ni^{(3+\delta)+}$ oxidation peak, (c) OER activity, and (d) TOF_{redox} at 1.53 V_{RHE} (300 mV overpotential) normalized to the number of electrochemically accessible Ni sites assuming an electron transfer number per active site of 1.7 for L1-based MHOFs and 1 for L4-based MHOFs (see Supporting Note 1 for more information). Electrodes were composed of 125 μg_{MHOF} $cm_{geo.}^{-2}$ and 14 μg_{Nafion} $cm_{geo.}^{-2}$ on a 0.196 cm^2 glassy carbon disk. A calibrated Hg/HgO reference electrode was used with a Pt wire counter electrode.

RESULTS AND DISCUSSION

Electrochemical Activation of MHOFs. The structures of the investigated MHOFs showing the carboxylate linkers (L1, L4) in the interlayer spacing are shown in Figure 1a,b. The pre-OER Ni redox peaks centered around 1.4 V_{RHE} as well as the OER current of the MHOFs ($Ni_2(OH)_2$(L1), Fe/$Ni_2(OH)_2$(L1), $Ni_2(OH)_2$(L4), and Fe/$Ni_2(OH)_2$(L4)) are shown in Figure 1c–f, which were found to change greatly during CV cycling at 10 mV s^{-1} between 1.1 and 1.7 V_{RHE} in 0.1 M KOH. The equilibrium Ni redox potential (defined as the average between the peak potential at the maximum peak current of oxidation or reduction) was found to shift positively by ~60, 50, and 20 mV for $Ni_2(OH)_2$(L1), Fe/$Ni_2(OH)_2$(L1), and $Ni_2(OH)_2$(L4), respectively, from the 25th to 500th cycle (Figures 2a, S2 and S3). On the other hand, Fe/$Ni_2(OH)_2$(L4) exhibited negligible shifts in the equilibrium redox potential during cycling. Moreover, the increasing pre-OER Ni redox peaks upon CV cycling indicate that more Ni progressively became electrochemically accessible, which was inferred by the charges contained in the Ni oxidation peaks (see Supplementary Note 1 for extraction of redox charges). The geometric charge density of Ni redox of $Ni_2(OH)_2$(L1) increased rapidly, reaching a maximum after cycle 25, which gradually decreased during subsequent cycles (Figure 2b). Fe/$Ni_2(OH)_2$(L1) was found to exhibit a similar trend but with a smaller increase in the Ni redox charge, approximately ~50% that of $Ni_2(OH)_2$(L1). On the other hand, the geometric Ni redox charge of $Ni_2(OH)_2$(L4) and $FeNi_2(OH)_2$(L4) was found to increase gradually with cycle number and reached similar values after 500 cycles in Figure 2b. The percentage of electrochemically accessible Ni sites based on the nominal mass loading and the total Ni oxidation charge as a function of cycle number are shown in Figures S3 and S4, respectively. We also tested $Ni_2(OH)_2$(L4) and Fe/$Ni_2(OH)_2$(L4) loaded on acid-treated acetylene black to investigate whether a carbon support suppresses the observed activation; however, similar results to those of the unsupported catalysts were observed (Figure S5). Lastly, to rule out that the activation of these MHOFs during CV cycling is not due to trace Fe impurities from the electrolyte or from the glass cell, which has been previously demonstrated for Ni (oxy)hydroxides,[28,29] we repeated the cycling measurements with $Ni_2(OH)_2$(L4) and Fe/$Ni_2(OH)_2$(L4) in purified 0.1 M KOH using an acid-cleaned PTFE cell (Figure S6). Activation similar to that observed in the presence of Fe impurities was also noted in Fe-free electrolyte, effectively excluding Fe impurities as the sole cause of activation. The origin of this activation will be further explored in the following sections.

The geometric OER activity of $Ni_2(OH)_2$(L1) in Figure 1c and Fe/$Ni_2(OH)_2$(L1) in Figure 1e increased by about an order of magnitude while the activity of L4 analogues in Figure 1d,f was enhanced by about 2 orders of magnitude, as measured at 1.53 V_{RHE} before and after 500 CV cycles at 10 mV s^{-1} between 1.1 and 1.7 V_{RHE} (Figures 2c and S7). While $Ni_2(OH)_2$(L1) and Fe/$Ni_2(OH)_2$(L1) reached the maximum OER activity after ~25 cycles, which remained largely unchanged upon subsequent cycling, the $Ni_2(OH)_2$(L4) and Fe/$Ni_2(OH)_2$(L4) catalysts showed continuous growth in the geometric OER activity during CV cycling. Furthermore, no changes in the Tafel slopes were observed for all MHOF studied, suggesting that the OER mechanism does not change significantly with increasing cycle number (Figure S7).

TOF_{redox} of the MHOFs as a function of cycle number was calculated to track the change in activity on a per active site

https://doi.org/10.1021/acs.chemmater.3c00316
Chem. Mater. XXXX, XXX, XXX−XXX

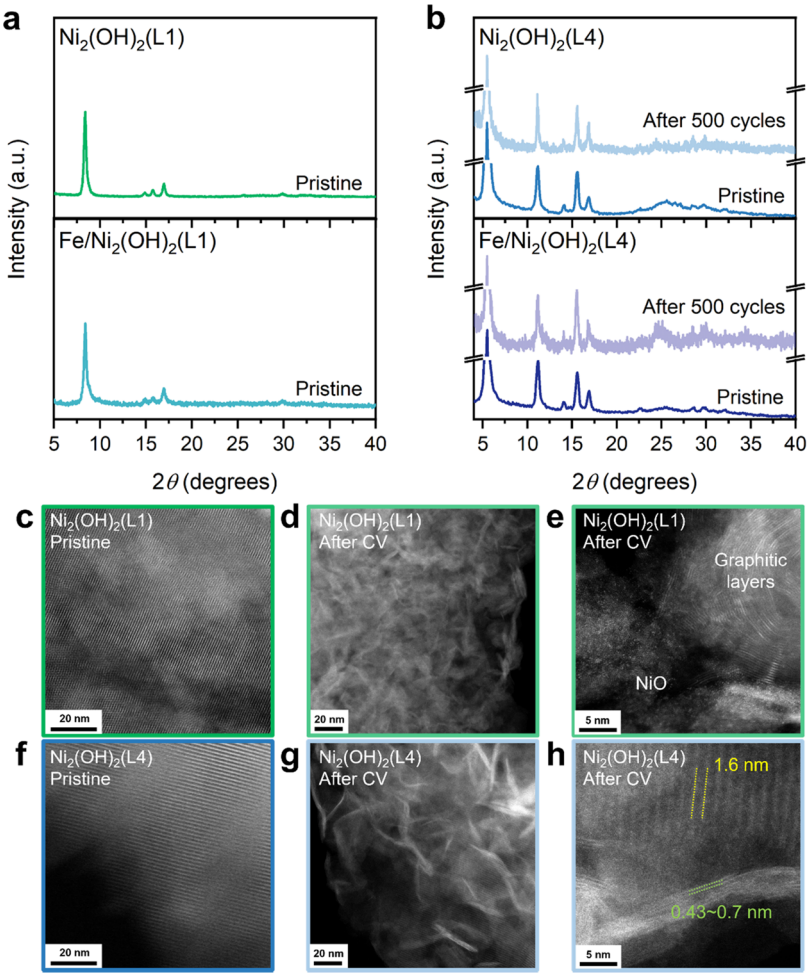

Figure 3. Powder X-ray diffraction (Cu anode, λ = 1.5418 nm) of (a) $Ni_2(OH)_2$(L1) (top) and Fe/$Ni_2(OH)_2$(L1) (bottom) and (b) Fe/$Ni_2(OH)_2$(L4) (top) and Fe/$Ni_2(OH)_2$(L4) (bottom) before and after 500 CV cycles from 1.1 to 1.7 V_{RHE}. Cyclic voltammetry tests were conducted at 1600 rpm at 10 mV s^{-1} in an O_2-saturated 0.1 M KOH electrolyte and ended at 1.1 V_{RHE}. Electrodes were composed of 6.25 mg_{MHOF} $cm_{geo.}^{-2}$ and 0.7 mg_{Nafion} $cm_{geo.}^{-2}$ on 8 cm^2 porous carbon felt electrodes. ADF-STEM images of MHOF nanosheets. $Ni_2(OH)_2$(L1) in the (c) pristine state and (d, e) after 500 OER CV cycles between 1.1 and 1.7 V_{RHE}. $Ni_2(OH)_2$(L4) in the (f) pristine state and (g, h) after 500 OER CV cycles between 1.1 and 1.7 V_{RHE}. Electrodes were composed of 125 μg_{MHOF} $cm_{geo.}^{-2}$ and 14 μg_{Nafion} $cm_{geo.}^{-2}$ on a 0.196 cm^2 glassy carbon disk. For all tests, a Hg/HgO reference electrode was used with a Pt wire counter electrode. Final cycles were terminated at 1.1 V_{RHE}, and electrodes were removed from the electrolyte within ~2 h of completing OER cycling.

basis of the MHOFs. Previous studies have shown that different phases of $Ni(OH)_2/NiOOH_{2-x}$ phase transformation are associated with different electron transfers per Ni ion.[30−32] We calculated the TOF_{redox} using both 1.7 e- per Ni (which is associated with the α-$Ni(OH)_2/\gamma$-$NiOOH_{2-x}$ transformation) and 1 e^- per Ni (which is associated with the β-$Ni(OH)_2/\beta$-$NiOOH_{2-x}$ transformation) as upper and lower bounds for the TOF_{redox}, respectively, as shown in Figure S8. However, our Raman measurements, which are discussed in detail below, suggest that the L1-based MHOFs are transforming to the γ-$NiOOH_{2-x}$ phase, whereas the L4-based MHOFs are transforming to the β-$NiOOH_{2-x}$ phase.[26] Therefore, TOF_{redox} values are reported using 1.7 e^- per Ni in the L1-based MHOFs and 1 e^- per Ni in the L4-based MHOFs (see Supporting Note 1 for more details). The TOF_{redox} for Fe/$Ni_2(OH)_2$(L1) and Fe/$Ni_2(OH)_2$(L4) were found nearly unchanged upon CV cycling, while that of $Ni_2(OH)_2$(L1) and $Ni_2(OH)_2$(L4) decreased rapidly in the first 25 cycles. Although the TOF_{redox} of $Ni_2(OH)_2$(L4) reached a plateau after ~200 cycles, the TOF_{redox} of $Ni_2(OH)_2$(L1) kept increasing with subsequent cycling. The higher geometric OER activity and TOF_{redox} for MHOFs with Fe incorporation are in agreement with previous works of oxide-derived NiFe catalysts.[19,21,23] The higher geometric OER activity in Figure 2c and TOF_{redox} in Figure 2d for $Ni_2(OH)_2$(L1) than $Ni_2(OH)_2$(L4) can be attributed to greater transformation to $NiOOH_{2-x}$, which can be facilitated by faster leaching of L1 linkers from $Ni_2(OH)_2$(L1) in 0.1 M KOH than L4 linkers in $Ni_2(OH)_2$(L4) due to weaker $\pi-\pi$ interactions.[19] Furthermore, Fe/$Ni_2(OH)_2$(L1) was the most active at cycle 500, with a TOF_{redox} of 2.4 s^{-1} followed by Fe/$Ni_2(OH)_2$(L4), with a TOF_{redox} of 1.3 s^{-1} at cycle 500, which are among the most active oxide-derived NiFe OER catalysts.[21] We note that this analysis requires further work to elucidate the origin of the enhanced TOF_{redox}, especially for the L1-based material, as the OER activity of such MHOFs can be greatly influenced by the degree of surface and bulk transformations. Moreover, not all Ni sites have comparable OER activity as recent work has shown that active sites can be limited to undercoordinated surface sites.[33−35] $Ni_2(OH)_2$(L1) and $Ni_2(OH)_2$(L4) were also studied using chronopotentiometry measurements, which are discussed in Figure S9.

https://doi.org/10.1021/acs.chemmater.3c00316
Chem. Mater. XXXX, XXX, XXX−XXX

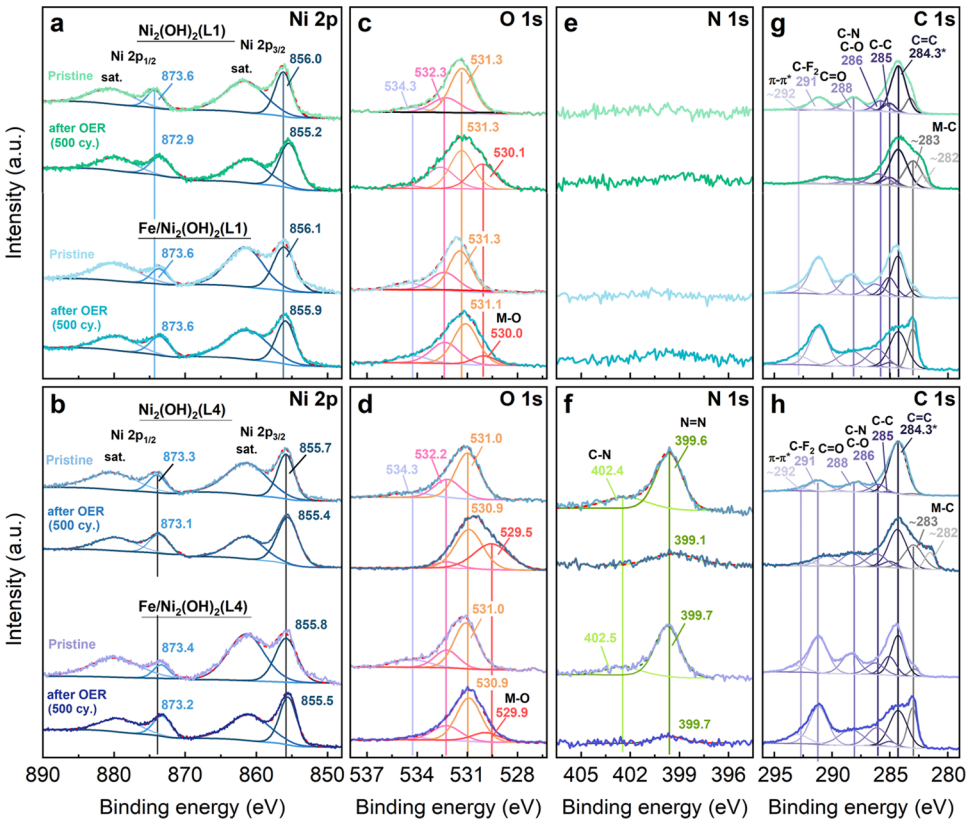

Figure 4. XPS spectra of MHOFs before and after CV cycling in 0.1 M KOH used without further purifications. (a, b) Ni 2p, (c, d) O 1s, (e, f) N 1s, and (g, h) C 1s. From top to bottom in each figure: $Ni_2(OH)_2$(L1), $Fe/Ni_2(OH)_2$(L1) or $Ni_2(OH)_2$(L4), and $Fe/Ni_2(OH)_2$(L4). MHOFs containing the L1 linker are shown in the top row (a, c, e, g) and MHOFs with the L4 linker are shown in the bottom row (b, d, f, h). The CV cycling was performed on the MHOFs with a loading of 125 μg_{MHOF} $cm_{geo.}^{-2}$ and 14 μg_{Nafion} cm_{geo}^{-2} dispersed on a glassy carbon electrode between 1.1 and 1.7 V_{RHE} at 10 mV s^{-1}. The cycling was terminated in the reduced state (1.1 V_{RHE}).

Using a different upper potential limit of CV cycling from 1.37, 1.55, and 1.7 V_{RHE}, the Ni oxidation peak of $Ni_2(OH)_2$(L4) was found to grow, while the geometric OER activity was shown to decrease with increasing upper voltage limit. For example, cycling $Fe/Ni_2(OH)_2$(L4) up to 1.37 V_{RHE} (prior to the pre-OER Ni redox) peak showed a smaller Ni redox peak area than the electrodes cycled to 1.70 V_{RHE} after 500 cycles. Uncycled electrodes (exposed to 0.1 M KOH at open circuit) showed even lower Ni redox peaks than those cycled to 1.37 V_{RHE} (Figure S10a). Moreover, after a fixed time of cycling of 450 min (i.e., different cycle numbers) with an upper potential bound of 1.37, 1.55, and 1.70 V_{RHE} (Figure S10b), similar Ni oxidation peak size and OER activity were observed for all electrodes, suggesting that exposure time at voltages greater than 1.37 V_{RHE} was important to activate the electrochemically active surface area of Ni and indicating that the degree of transformation of MHOFs is a stronger function of exposure time to the 0.1 M KOH electrolyte than on oxidizing potential.

Long-Range Order and Local Atomic Characterization of MHOFs after OER Cycling. To understand the structural changes of the MHOFs after OER cycling, we analyzed the materials using bulk and surface-sensitive techniques. Since $Ni_2(OH)_2$(L1) and $Fe/Ni_2(OH)_2$(L1) were unstable in 0.1 M KOH, sufficient material was not collected after electrochemical cycling for XRD, in agreement with previous studies.[36] X-ray diffraction of $Ni_2(OH)_2$(L4) and $Fe/Ni_2(OH)_2$(L4) (Figure 3b) revealed negligible changes after 710 cycles (~18 h) between 1.1 and 1.55 V_{RHE}, indicating that the bulk structure remained largely unchanged and structural transformations near the surface were responsible for the observed changes during CV cycling (Figure 3b). We further investigated the structural and morphological changes of these MHOFs using STEM. ADF and iDPC-STEM images (Figure 3c) confirmed the layered structure and morphology of pristine $Ni_2(OH)_2$(L1) and $Fe/Ni_2(OH)_2$(L1) with an atomic plane spacing of 1.06 nm that is characteristic to L1 (Figures S11a, S12a) and in agreement with previous work.[19] Considerable structural and morphological changes of $Ni_2(OH)_2$(L1) were observed after 500 cycles from 1.1 to 1.7 V_{RHE}. Not only did the original layered structure of $Ni_2(OH)_2$(L1) disappear (Figure 3d,e), but cycled $Ni_2(OH)_2$(L1) was observed to exhibit crumpled features (Figure 3d), which could be attributed to significant structural transformations. A Fourier transform of the image (Figure S13) suggests the formation of NiO phases with various domain sizes ranging from a few nm^2 to hundreds of nm^2, which could result from linker leaching from $Ni_2(OH)_2$(L1) in the electrolyte, transforming to $NiOOH_{2-x}$,[36] and decomposing to NiO-like phases, accompanied by the rapid increase in redox peak areas and OER activity during CV cycling (Figure 2c,d). In addition, BF-STEM images (Figure S14a) revealed layered spacings of ~0.33 nm, which are attributed to graphite-like domains from electron energy loss spectroscopy (Figure S14b) and presumably from the leaching of linkers and subsequent redeposition of carbon derived from linkers. Similar phenomena were found in cycled $Fe/Ni_2(OH)_2$(L1),

https://doi.org/10.1021/acs.chemmater.3c00316
Chem. Mater. XXXX, XXX, XXX−XXX

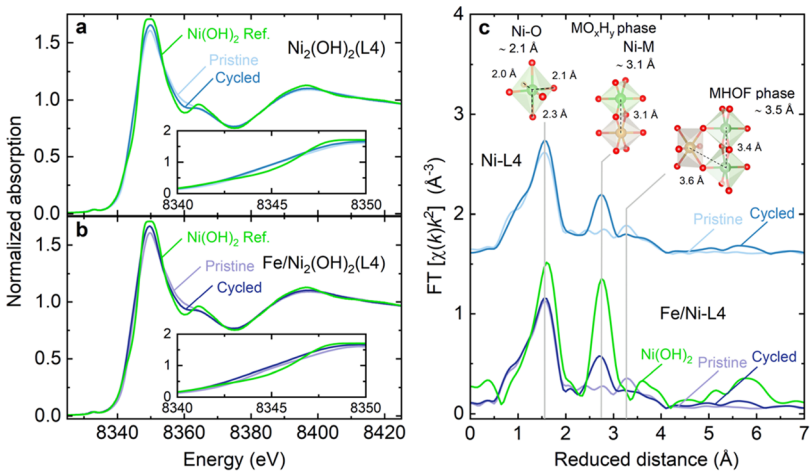

Figure 5. X-ray absorption spectroscopy of pristine and cycled $Ni_2(OH)_2$(L4) and Fe/$Ni_2(OH)_2$(L4) MHOF nanosheets. X-ray absorption near-edge spectroscopy (XANES) of the Ni *K*-edge for pristine and cycled (a) $Ni_2(OH)_2$(L4) and (b) Fe/$Ni_2(OH)_2$(L4) MHOF nanosheet compositions. β-$Ni(OH)_2$ reference spectra are shown in green. Insets in each plot show an enlarged view of the rising edge from 8340 to 8350 eV. (c) k^2-weighted FT-EXAFS of $Ni_2(OH)_2$(L4) (top) and Fe/$Ni_2(OH)_2$(L4) (bottom) in the pristine and after cycling of 710 cycles from 1.1 to 1.55 V_{RHE} in 0.1 M KOH used without further purification (after 18 h). The lower upper vertex potential was used to decrease bubble formation from the increased catalyst loading and extended cycling. A $Ni(OH)_2$ standard is shown in green. Electrodes were composed of 6.25 mg_{MHOF} $cm_{geo.}^{-2}$ and 0.7 mg_{Nafion} $cm_{geo.}^{-2}$ on 8 cm^2 porous carbon felt electrodes. Electrode cycling was terminated at 1.1 V_{RHE} and removed from the electrolyte within ~2 h of completion.

showing NiO/FeO domains and graphitic layers (Figure S12b,c).

The layered structure and sheet-like morphologies of $Ni_2(OH)_2$(L4) (Figures 3f and S11b) exhibited crumpled characteristics with the layered structure remaining underneath after 500 cycles, indicating that the structural and morphological transformations occur only in the near-surface region (Figure 3g,h), contrary to the bulk structure transformation observed for the L1-based MHOFs. The atomic plane spacing of 1.6 nm present in the pristine $Ni_2(OH)_2$(L4) was still present after cycling (Figure 3h), demonstrating that the bulk structure of $Ni_2(OH)_2$(L4) remained intact and agrees with the XRD results. $NiOOH_{2-x}$-like domains were formed in the surface regions of cycled $Ni_2(OH)_2$(L4) (Figure 3h) instead of NiO-like domains found for cycled $Ni_2(OH)_2$(L1), where layered spacings in the range from 0.43 to 0.70 nm (primarily 0.45 nm) were measured, which matches closely with the ~0.46 and ~0.70 nm interlayer spacings found in β-$Ni(OH)_2$ and γ-NiOOH, respectively.[37,38] Unlike with cycled $Ni_2(OH)_2$(L1), graphite and carbon-like structural features were not observed in the cycled $Ni_2(OH)_2$(L4) materials. The restructuring observed for $Ni_2(OH)_2$(L1) and $Ni_2(OH)_2$(L4) after 500 OER cycles between 1.1 and 1.7 V_{RHE} explains the electrochemical data in Figure 2b showing a significant increase in the electrochemically active Ni sites with increasing cycle number. As seen in Figure S12d−f, the structural and morphological transformation in Fe/$Ni_2(OH)_2$(L4) has similar features to the $Ni_2(OH)_2$(L4) sample, showing the heterostructure formation of intact MHOF and $NiOOH_{2-x}$ redox active structures.

X-ray photoelectron spectroscopy (XPS) was used to reveal chemical composition changes of the MHOFs before and after CV cycling. The Ni $2p_{1/2}$ and Ni $2p_{3/2}$ peaks of pristine $Ni_2(OH)_2$(L1) and $Ni_2(OH)_2$(L4) were centered at binding energies of ~873 and ~856 eV (Figures 4a,b and S15), respectively, indicative of Ni^{2+}.[19,39,40] Fe substitution in Fe/$Ni_2(OH)_2$(L1) and Fe/$Ni_2(OH)_2$(L4) had negligible changes in the binding energy, in good agreement with Fe substitution in $NiOOH_{2-x}$-like[36,41] and MOF phases.[16] There was a noticeable small shift of the Ni 2p peaks to lower binding energy (~0.8 eV) after cycling of $Ni_2(OH)_2$(L1), which could be explained by the formation of NiO (Figure S16), which is known to have lower binding energy than that of $Ni(OH)_2$ and $Ni_2(OH)_2$(L1).[39,40] Unfortunately, the quantification in the Ni oxidation state changes before and after CV cycling was inclusive due to the small peak shifts observed (Figure S17) and intrinsically similar binding energies of Ni 2p peaks for Ni^{2+}, Ni^{3+}, and Ni^{4+}.[40−42] The satellite peaks are likely associated with Ni^{2+} or Ni^{3+} species due to multiple splitting effects from the unpaired d-electrons in these species.[40,41] The satellite peaks were found to decrease in intensity after cycling, which may suggest oxidation to higher valent $Ni^{(3+\delta)+}$ states or a modified local electron density due to loss of linker after exposure to voltages up to 1.7 V_{RHE}. The Fe 2p spectrum had negligible intensities for the Fe/$Ni_2(OH)_2$(L1) and Fe/$Ni_2(OH)_2$(L4) samples both before and after cycling (Figure S18b), meaning the surface Fe-content was low and could not be accurately quantified. Based on previous studies the Fe-content is well below 5 atom %,[23] which is significantly lower than the bulk Fe-content (~15 atom %) estimated from both ICP-MS and SEM-EDX (Tables S1−S3 and Figures S19−S21). The reason for this discrepancy is still unclear. Similar changes were observed for carbon-supported $Ni_2(OH)_2$(L1) and Fe/$Ni_2(OH)_2$(L4) cycled in a purified electrolyte (Figure S18), further supporting that enhanced redox peaks and OER activity is not originating from Fe accumulation/contamination in the catalysts upon cycling. Moreover, the O 1s spectra of pristine $Ni_2(OH)_2$(L1) and Fe/$Ni_2(OH)_2$(L1) in Figure 4c and pristine $Ni_2(OH)_2$(L4) and Fe/$Ni_2(OH)_2$(L4) (Figure 4d) had three components at ~534.4, 532.3, and 531.0 eV, which we assign to C-O, O=C−O or H_2O, and M−OH, respectively. After CV cycling, an additional peak at 530 eV was noted for all cycled MHOFs, which could be attributed to metal-oxo (M-O) groups. Additional peaks appeared at ~283 and 281.5 eV in the C 1s spectra after cycling in the pure Ni MHOF catalysts, attributable to nickel carbide (Ni-C) species

https://doi.org/10.1021/acs.chemmater.3c00316
Chem. Mater. XXXX, XXX, XXX−XXX

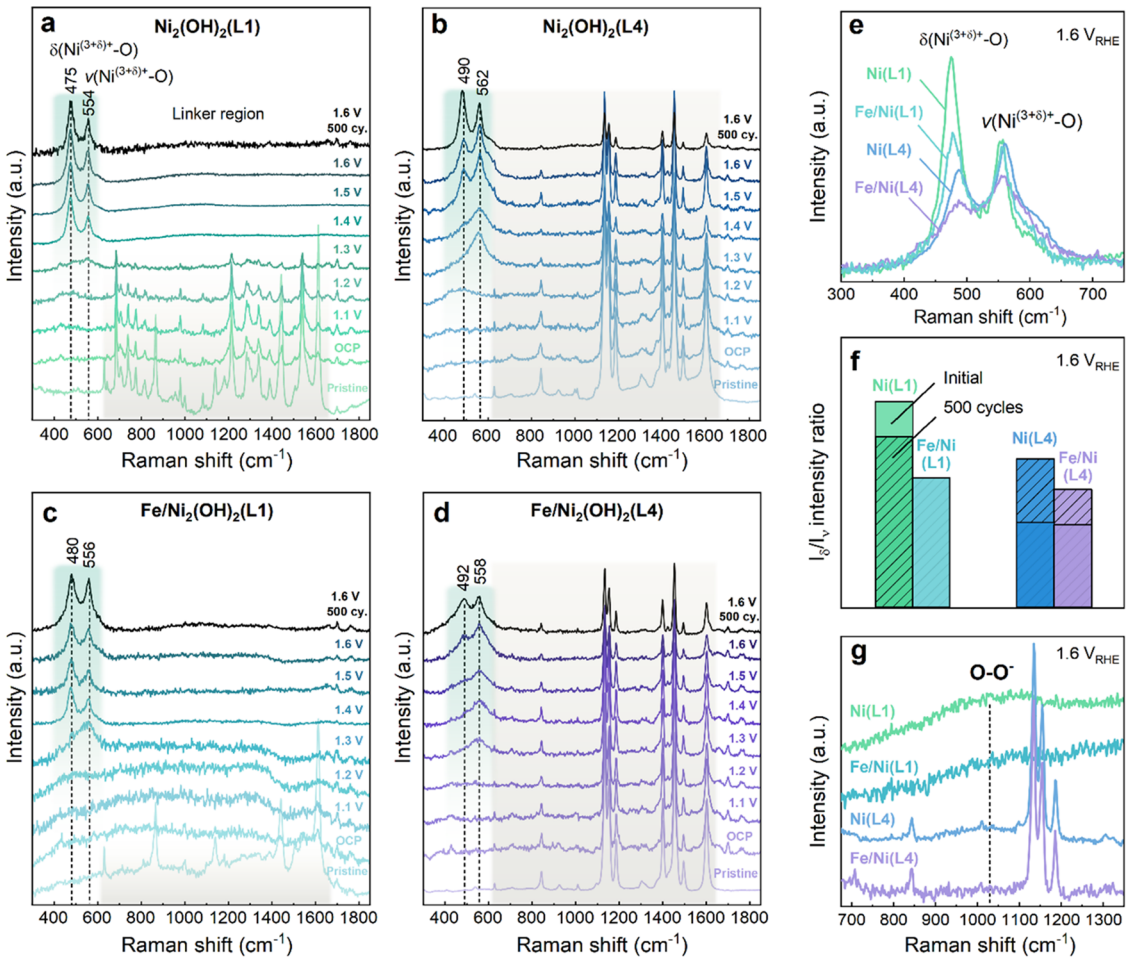

Figure 6. In situ Raman spectroscopy of MHOFs: (a) $Ni_2(OH)_2$(L1), (b) $Ni_2(OH)_2$(L4), (c) Fe/$Ni_2(OH)_2$(L1), and (d) Fe/$Ni_2(OH)_2$(L4). (e) Comparison of selected spectra at 1.6 V_{RHE} before the extended cycling. (f) Relative I_δ and I_ν peak intensities before and after 500 cycles at 1.6 V_{RHE} and (g) enlargement of the superoxo ($NiOO^-$) region at 1.6 V_{RHE} before extended cycling. Spectra were recorded during steady-state conditions. The laser excitation wavelength was 633 nm, and the catalysts were investigated on roughened SERS-active bulk Au electrodes in purified 0.1 M KOH. The spectra in (e) were normalized to the minimum between the two I_δ and I_ν bands to facilitate comparison of the relative intensities.

(Figure 4g).[43] The lowest B.E. peak at 281.5 eV was consistently absent in both Fe-doped MHOFs, suggesting that Fe prevents the formation of this species. Furthermore, a significant intensity reduction of the components at ~402.4 and 399.6 eV in the N 1s spectra of cycled $Ni_2(OH)_2$(L4) and Fe/$Ni_2(OH)_2$(L4) (Figure 4f) confirms leaching of C−N and N═N groups of the L4 linker (azobenzene-4,4′-dicarboxylate)[44] (Table S2). Our XPS results suggest that transformations toward $NiOOH_{2-x}$-like phases are initiated at the surface of the MHOFs along with structurally developed new M−O moieties not present in the pristine MHOF structure. Our XPS results align with previous analysis of nickel-based MOF materials which undergo phase conversion to (oxy)-hydroxide in base.[45,46]

X-ray absorption spectroscopy (XAS) at the Ni *K*-edge was employed to probe changes in local atomic structure and identify the transformed structure of $Ni_2(OH)_2$(L4) and Fe/$Ni_2(OH)_2$(L4) upon cycling from 1.1 to 1.55 V_{RHE} (Figure 5). The Ni *K*-edge data confirmed the presence of Ni^{2+} for pristine $Ni_2(OH)_2$(L4) in Figure 5a and Fe/$Ni_2(OH)_2$(L4) in Figure 6b (Table S4), in agreement with previous work (Figure S22 shows the calibration curve used to determine Ni oxidation states from reference compounds).[19] After cycling, a small shift in the Ni *K*-edge energy toward lower energy by 0.1 and 0.6 eV was found for cycled $Ni_2(OH)_2$(L4) and Fe/$Ni_2(OH)_2$(L4), respectively. The extended X-absorption fine structure (EXAFS) spectra were modeled using scattering paths generated in FEFF (Figures S23 and S24), where the magnitude of the Fourier transformed EXAFS (FT-EXAFS) data are shown in Figure 5c. The intensity related to the coordination of Ni-Ni or Ni-M paths at ~3.10 Å was found to considerably grow (Figure 5c) for $Ni_2(OH)_2$(L4) and Fe/$Ni_2(OH)_2$(L4) after CV cycling, matching with the distance expected for layered $NiOOH_{2-x}$-like phases.[37,47] These findings are in agreement with reports of other MOF-derived materials and are consistent with the formation of $NiOOH_{2-x}$ phases after electrochemical cycling in base.[18,46] In addition, the average Ni-O bond distance in the first shell of the materials was found to expand from ~2.05 to ~2.10 Å after cycling (Table S5, S6). Using the unique Ni coordination environments found in the MHOF phase (Figure S25), linear combination fitting (LCF) of the *k*-space revealed that cycled $Ni_2(OH)_2$(L4) was composed of 38 atom % $Ni(OH)_2$ and 62 atom % $Ni_2(OH)_2$(L4), while cycled Fe/$Ni_2(OH)_2$(L4) was composed of 27 atom % $Ni(OH)_2$ and 73 atom % Fe/$Ni_2(OH)_2$(L4), which is in agreement with the LCF modeling

https://doi.org/10.1021/acs.chemmater.3c00316
Chem. Mater. XXXX, XXX, XXX−XXX

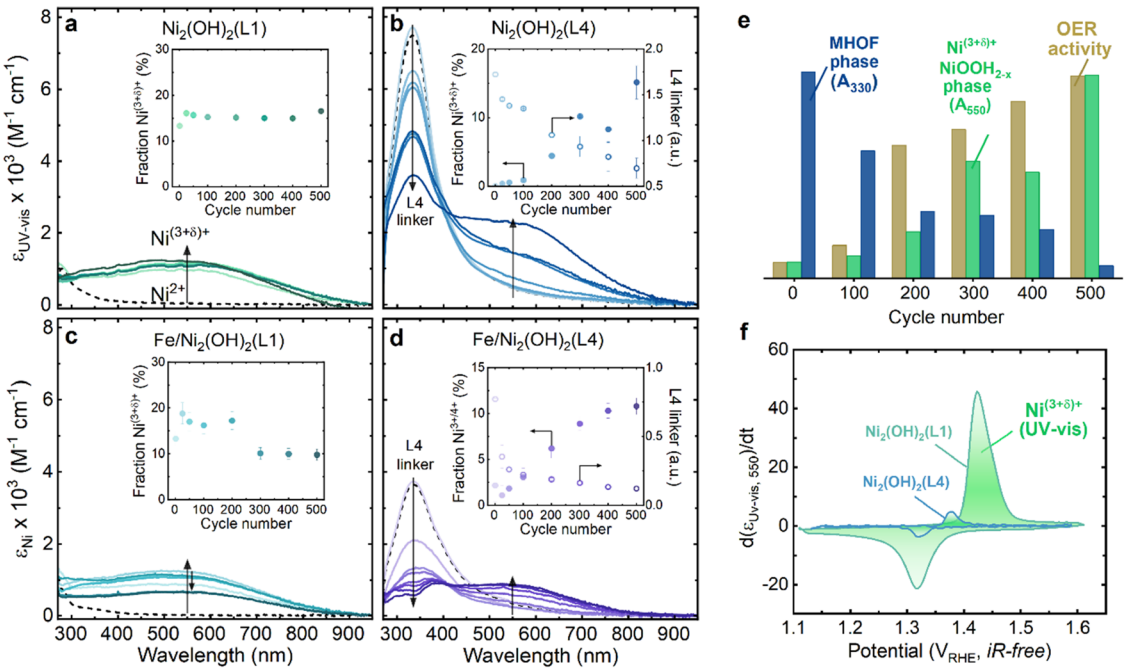

Figure 7. In situ UV−vis of MHOF catalysts up to 500 cycles. The molar extinction coefficient for (a) $Ni_2(OH)_2$(L1), (b) $Ni_2(OH)_2$(L4), (c) Fe/$Ni_2(OH)_2$(L1), and (d) Fe/$Ni_2(OH)_2$(L4). The insets show the fraction of $Ni^{(3+\delta)+}$ deduced from the UV−vis CT band at 550 nm. (e) Correlations between the L4 linker absorption band at 330 nm, the $Ni^{2+}/Ni^{(3+\delta)+}$ CT band at 550 nm, and the OER activity of the $Ni_2(OH)_2$(L4) catalyst. (f) Derivative of the UV−vis absorbance at 550 nm of the $Ni_2(OH)_2$(L1) and the $Ni_2(OH)_2$(L4) catalysts monitored during a CV sweep at 2 mV s^{-1} at relatively early stages of cycling (after ca. 1 h of "aged" state). The green shaded areas represent high-valence $Ni^{(3+\delta)+}$ states.

of the Ni *K*-edge for the materials (Figure S26). No contributions from metallic Ni foil or NiO were noted (more details are provided in Supporting Note 3 and Figure S27). Previous atomic force microscopy measurements of L4-based MHOF nanosheets synthesized identically to the ones studied here showed a thickness of ∼4.2 nm or ∼12 unit cells.[19] Therefore, we estimate that ca. 0.5−0.8 nm, or ca. 2−3 unit cell layers, on each plane of the nanosheet are transforming from the MHOF to $NiOOH_{2-x}$-like structure when cycled between 1.1 and 1.55 V_{RHE} at 10 mV s^{-1}. In other words, about 0.5−0.6% of the layers are transforming from the MHOF structure to one resembling that of $NiOOH_{2-x}$ per cycle. These observations along with X-ray diffraction and STEM imaging results point to linker leaching and gradual structural transformations of $Ni_2(OH)_2$(L4) with and without Fe substitution into $NiOOH_{2-x}$ initiating at the near the surface regions.

In Situ Characterization of MHOFs as a Function of Potential. To understand the mechanism through which the MHOF phase evolves during electrochemical cycling, SERS was employed to track the structural evolution of $Ni_2(OH)_2$(L1), Fe/$Ni_2(OH)_2$(L1), $Ni_2(OH)_2$(L4), Fe/$Ni_2(OH)_2$(L4) in Figure 6a−d, respectively, as a function of potential. For all four MHOF catalysts, at potentials below 1.3 V_{RHE}, no bands are visible between 400 and 600 cm^{-1}. At potentials above the threshold of $Ni^{2+}/Ni^{(3+\delta)+}$ redox (1.4 V_{RHE}), two peaks emerged near ∼480 and 555 cm^{-1}, which are characteristic of $NiOOH_{1-x}$ phases.[24,29,48−51] These correspond to the E_g bending (δ) and A_{1g} stretching (ν) vibrational modes of layered $NiOOH_{2-x}$-like phases (Ni-O modes parallel to and perpendicular to the layers, respectively).[49] This suggests the formation of $NiOOH_{2-x}$-like phases in the MHOF catalysts, in accord with previous observations in other MOF materials.[45,52] The Raman intensity is sensitive to structural disorders, such as defects and vacancies,[53] while the peak positions are particularly sensitive to the Ni oxidation state.[26,53,54] At 1.6 V_{RHE}, the relative I_δ/I_ν intensity ratio is significantly larger for the two L1 MHOFs compared to the two L4 MHOFs (Figure 6e). Further, Fe substitution lowered the I_δ/I_ν ratio for MHOFs with both L1 and L4 linkers, which aligns with previous work suggesting that Fe incorporation in $Ni(OH)_2$ increases the structural disorder.[27,54] The lower I_δ/I_ν intensity ratio for both the L4 MHOFs indicates a higher structural disorder or a lower Ni oxidation state compared to the MHOFs employing the L1 linker.[54] After 500 CV cycles in 0.1 M KOH, the I_δ/I_ν ratio of the $Ni_2(OH)_2$(L1) and Fe/$Ni_2(OH)_2$(L1) showed negligible changes (Figures 6f and S28a,b), while the I_δ/I_ν ratio for both $Ni_2(OH)_2$(L4) and Fe/$Ni_2(OH)_2$(L4) grew with cycling (Figures 6f and S28c,d). This supports a gradual transformation toward $NiOOH_{2-x}$-like domains in all the MHOFs, although, this process seems to be faster and more significant in the L1 MHOFs.

Furthermore, the two primary δ and ν peaks are positioned at lower wavenumbers in the L1 MHOFs (575−580 cm^{-1}) compared to those in the L4-based MHOFs (590−592 cm^{-1}), which may be attributed to L1-based MHOFs preferentially transforming to that of α-$Ni(OH)_2/\gamma$-$NiOOH_{2-x}$ phases, whereas L4-based MHOFs tend to favor β-$Ni(OH)_2/\beta$-$NiOOH_{2-x}$ phases.[26] Previous studies of these phases of $NiOOH_{2-x}$ have shown that α-$Ni(OH)_2/\gamma$-$NiOOH_{2-x}$ phase changes are associated with ∼1.7 e^- transfers per Ni ion while β-$Ni(OH)_2/\beta$-$NiOOH_{2-x}$ phase changes are associated with ∼1 e^- per Ni ion,[30−32] motivating our choice of different electron transfer numbers per Ni site in the TOF_{redox} calculations. In the region between 900 and 1150 cm^{-1}, a broad band become noticeable in both the $Ni_2(OH)_2$(L1) and Fe/$Ni_2(OH)_2$(L1) MHOFs concomitant with the appearance of oxidized δ/ν-($Ni^{(3+\delta)+}$) bands (Figure 6a,b,g). This band has

https://doi.org/10.1021/acs.chemmater.3c00316
Chem. Mater. XXXX, XXX, XXX−XXX

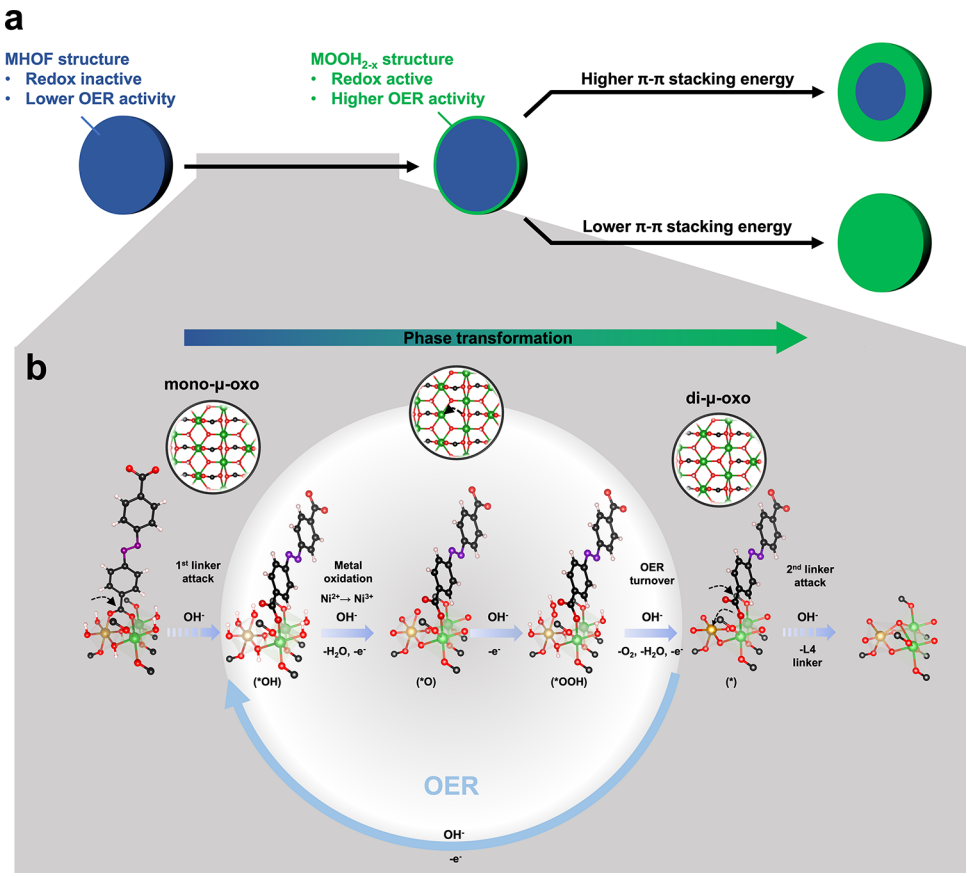

Figure 8. Mechanism of MHOF phase conversion (a) Morphological transformations of MHOFs when exposed to alkaline environments showing the difference between heterostructures. The transformation starts at the surface of the material irrespective of the linker toward $NiOOH_{2-x}$-like phases. MHOFs constructed using linkers with higher $\pi-\pi$ stacking energies lead to a core−shell-like structure where only an outer layer transforms with intact MHOF found within the core. MHOFs constructed using linkers with weaker $\pi-\pi$ interactions instead undergo complete transformation. (b) Proposed mechanistic scheme demonstrating the observed phase transformation of the MHOF to $NiOOH_{2-x}$-like phases, triggered by the loss of the organic linkers in the interlayer spacing, facilitated by the Ni redox as well as the high pH of the electrolyte, which results in loss of the MHOF-specific mono-μ-oxo motifs and the edge-sharing NiO_6 octahedra. The loss of linkers releases new sites potentially active for OER; however, these sites are not stable under the prevalent conditions which instead convert into $NiOOH_{2-x}$-like phases via angle rearrangement and contractions of the metal−metal bond distances. Chemical steps are denoted by dashed arrows, while electrochemical steps are denoted by blue arrows. The L4 linker is used as a representative example. Green atoms represent Ni, brown atoms represent Fe, red atoms represent O, black atoms represent C, purple atoms represent N, and gray atoms represent H.

been attributed to Ni species with superoxo character (NiO_2^-),[24,48] which provides additional evidence for the formation of $NiOOH_{2-x}$-like phases in the L1-based MHOFs. These broad superoxo bands are not observed in the L4 analogues, suggesting that the concentration of the species is either low or absent. Figure S29 shows the OER activity and Ni oxidation charge of MHOFs before and after cycling in the Raman cell; similar trends are observed as those in Figures 1c−f and 2.

The Raman bands between ca. 600 and 1700 cm^{-1} corresponding to the carboxylate linkers were used to monitor linker stability in the MHOF structure as a function applied potential and after cycling. After just immersing in the 0.1 M KOH electrolyte, the intensity of the L1 linker bands of $Ni_2(OH)_2$(L1) and $Fe/Ni_2(OH)_2$(L1) was found to significantly decrease even without an applied potential, whereas the L4 linker bands of $Ni_2(OH)_2$(L4) and $Fe/Ni_2(OH)_2$(L4) remained largely unaffected by the same treatment (Figures 6 and S30). Beyond 1.4 $V_{RHE,}$ the remaining L1 linker bands irreversibly disappear, suggesting that the formation of $Ni^{(3+\delta)+}$ facilitates the leaching of linkers in $Ni_2(OH)_2$(L1) and $Fe/Ni_2(OH)_2$(L1) MHOFs (Figure 6a,c), in agreement with previous studies.[37,55] On the other hand, the L4 linker bands for $Ni_2(OH)_2$(L4) and $Fe/Ni_2(OH)_2$(L4) MHOFs (Figure 6b,d) remain mostly intact up to 1.7 V_{RHE} for 500 cycles (~14 h of cycling), save for a small decrease in the intensity. These observations, coupled with the fact that the I_δ/I_ν ratio of the L4 MHOFs is consistently smaller than their L1 analogues, suggest that the transformation from MHOF to $NiOOH_{2-x}$-like phases occurs more rapidly in the L1-based MHOFs. This difference in transformation rate can be explained by more facile leaching of the L1 than the L4 linker when exposed to the 0.1 M KOH electrolyte, compared to the L4 linker. These results further corroborate the XRD, STEM, and XPS data, positing a gradual transformation from MHOF to $NiOOH_{2-x}$ phase progressing from the near-surface regions of our MHOF materials.

Using the electrochromic nature of $Ni^{(3+\delta)+}$ species, previous studies have shown that the broad absorption peak centered around 550 nm, attributed directly to the charge transfer (CT) between oxygen ligands and oxidized $Ni^{(3+\delta)+}$, can be used to track changes in the oxidation state of $NiOOH_{2-x}$.[22,27,56,57] By

https://doi.org/10.1021/acs.chemmater.3c00316
Chem. Mater. XXXX, XXX, XXX−XXX

observing that the derivative of the absorbance at 550 nm with respect to potential coincides with the Ni redox peak currents of the CV cycle, we can confirm this assignment (Figure S31). The L1 linker was not detected in our MHOFs as it has UV−vis absorption at ∼240 nm,[19] which is below the cutoff window of the FTO electrode. However, for the $Ni_2(OH)_2$(L4) and Fe/$Ni_2(OH)_2$(L4) MHOFs, an additional absorption peak at ∼330 nm was observed, which was assigned to the L4 linkers (Figure S32).[19] UV−vis spectra recorded every 100th cycle for 500 cycles revealed only a small increase in the CT band intensity for $Ni_2(OH)_2$(L1) (Figure 7a), but an initial increase followed by a slight decrease in CT band intensity for Fe/$Ni_2(OH)_2$(L1) (Figure 7c). The observed decrease in CT band intensity for Fe/$Ni_2(OH)_2$(L1) could be attributed to either loss of catalyst material from the electrode or possibly from the incorporation of Fe ions from the electrolyte, which could both lower the CT band.[27,28] Unlike the spectra for their L1 analogues, the $Ni_2(OH)_2$(L4) and Fe/$Ni_2(OH)_2$(L4) MHOFs did initially not display any prominent CT band during the first ∼200 cycles (Figure 7b,d). This can be attributed to the absence of significant amounts of $Ni^{(3+\delta)+}$, which may be due to a small percentage of transformed MHOF phase to $NiOOH_{2-x}$-like phases of the material (Figure 7f). Upon further cycling, the CT band at ∼550 nm for the L4-based MHOFs became gradually visible and grew in intensity with cycling, while the L4 absorption peak at ∼330 nm steadily decreased (Figures S33 and S34). The percentage of transformed MHOF phase after 500 cycles was estimated from the amount of $Ni^{(3+\delta)+}$ from the CT band and was between 10 and 20% depending on the MHOF and the linker (see Table S7).

As the OER activity increased with the increase in the CT band and the decrease of the L4 linker band (Figures S35 and S36), these observations provide further support that linker loss is essential for the transformation to $NiOOH_{2-x}$-like domains that are active for OER (as depicted in Figure 7e). Our UV−vis data strongly suggests that the MHOF phase is redox-inactive and is associated with OER-inactive or significantly higher overpotential, as evidenced by the inverse correlation between the L4 linker band and both the CT band intensity and the OER activity. Figure S37 provides a comparison of the OER activities and Ni oxidation charges of the MHOF catalysts in the UV−vis, revealing similar trends to those observed in Figures 1c−f and 2.

We summarize our findings in Figure 8. Our data shows that the partial loss of organic linkers is associated with the transformation to $NiOOH_{2-x}$-like phases near the surface regions of the MHOFs, where the degree of transformation is increased by weakening the $\pi-\pi$ stacking interaction of linkers (Figure 8a). Atomically, the transformation indicates loss of the NiO_6 corner-sharing octahedra and mono-μ-oxo motifs (Ni-(O)-M), leaving $NiOOH_{2-x}$-like phases composed of edge-sharing di-μ-oxo motifs (Ni-$(O)_2$-M) (Figure 8b), which is supported by STEM imaging, EXAFS, and in situ Raman measurements. Based on our electrochemical data and detailed ex situ and in situ characterization, we propose a possible mechanism for the enhanced OER activity by the phase transformation from MHOF to $NiOOH_{2-x}$ via loss of organic linkers (illustrated in Figures S38 and S39). This phase transformation process is spontaneous at open circuit potential, however, is facilitated by the Ni redox process. The linker loss may proceed via hydrolysis and is initiated by nucleophilic attack on the linker by base.[58,59] Since the pre-OER redox process occurs via deprotonation of nickel hydroxy to oxo ligands, the linkers must be lost instead of protons for the Ni centers to formally increase their oxidation states beyond Ni^{3+}, which may explain why the catalytic process may enhance loss of the linkers. This would further expose a greater number of coordinatively undercoordinated oxygen sites (i.e., μ_1-O or μ_2-O) throughout the bulk of the MHOFs (Figure S39). These presumed catalytic sites are typically only present at the "surface" (edge and corner sites) in $NiOOH_{2-x}$ phases.[33−35] Therefore, loss of linker could potentially increase the OER activity of the MHOFs, which is consistent with previous studies that have shown a correlation between missing linkers or defects and increased OER activity.[60,61] However, we observe that loss of linkers instead triggers the transformation of the MHOF toward $NiOOH_{2-x}$-like phases. Consequently, this transformation ultimately results in the loss of these newly formed coordinatively unsaturated and potentially catalytic sites within the MHOF phase (as illustrated in Figure 8). This involves loss of the MHOF-specific mono-μ-oxo domains, which subsequently convert to di-μ-oxo motifs. Given that this transformation, accompanied by the loss of MHOF-specific domains, is associated with an increase in the OER activity, we hypothesize that the resulting $NiOOH_{2-x}$ phases constitute the catalytic phase, wherein a greater proportion of $Ni^{(3+\delta)+}$ sites seems critical to efficiently catalyze OER.[14] The MHOF phases herein are hence only precatalysts.

Notably, assuming the most conventional proton-coupled electron transfer (PCET) OER mechanism, our previous density functional theory (DFT) calculations[19] of pristine Ni-based MHOF surfaces showed that their $Ni^{2+}/Ni^{(3+\delta)+}$ redox process corresponds to the deprotonation of surface $*H_2O$ to *OH adsorbates (with * indicating the surface metal sites). Moreover, the DFT-computed PCET OER energetics of such MHOF surfaces suggest that their rate-determining step is the further deprotonation of *OH to *O. Shifting the Ni redox of MHOF surfaces positively thus destabilizes *OH and leads to a lowered barrier for the rate-limiting *OH-to-*O transition. In contrast to pristine MHOFs, for pristine $NiOOH_{2-x}$ prior DFT investigations have suggested their $Ni^{2+}/Ni^{(3+\delta)+}$ redox corresponds to the transition from *OH-to *O-covered surfaces,[37] and this *OH to *O step limits the theoretical overpotential.[22] Facilitating Ni oxidation to Ni^{4+} in $NiOOH_{2-x}$ would therefore promote its intrinsic OER activity.[62] In addition, the enhanced conductivity of Ni^{3+} and Ni^{4+} states relative to the insulating Ni^{2+} state is also a critical factor. The higher conductivity facilitates the transfer of electrons (charge transfer) involved in the OER process and helps to ensure optimal performance.[23] Thus, by combining such prior insights with this study, we can suggest the dual functionality of organic linkers in modulating Ni oxidation and OER activity. Specifically, linkers with strong $\pi-\pi$ stacking energy are more effective at suppressing the phase transformation compared to linkers with weaker $\pi-\pi$ stacking energy. However, this stabilized MHOF phase is OER-inactive because the Ni^{2+} species cannot transfer charges efficiently.[23] The loss of organic linkers during electrochemical cycling not only transforms MHOF surfaces into $NiOOH_{2-x}$-like phases but also plays a critical role in enabling the oxidation of Ni^{2+} to $Ni^{(3+\delta)+}$, which is essential for efficient OER catalysis on MHOF-derived $NiOOH_{2-x}$ surfaces.

https://doi.org/10.1021/acs.chemmater.3c00316
Chem. Mater. XXXX, XXX, XXX−XXX

CONCLUSIONS

Our work reveals important details and unravels underlying processes causing loss of MHOF-specific motifs, and subsequent phase transformations from MHOF to $NiOOH_{2-x}$-like phases during alkaline OER, shedding new light onto the phase stability of these class of materials during OER in base. The comprehensive information regarding the phase transformation of MHOFs during highly oxidizing potentials marks a significant contribution to the field of electrocatalyst design utilizing inorganic-organic hybrid materials. To summarize, during electrochemical OER cycling, linkers leach from the MHOF structure, causing a transformation to $NiOOH_{2-x}$ phases, thereby exposing more electrochemically active Ni sites and increasing the OER currents. The linker leaching was observed to be accelerated by Ni^{2+} to $Ni^{(3+\delta)+}$ oxidation, leading to a phase transformation from MHOF to $NiOOH_{2-x}$ structure. A mechanistic transformation scheme is proposed where mono-μ-oxo bridge motifs found only in the MHOF structure convert to di-μ-oxo bridge motifs in the $NiOOH_{2-x}$-like phase, while MHOFs with the weaker $\pi-\pi$ interaction (such as the L1 linker) underwent complete and rapid transformation to $NiOOH_{2-x}$-like phases. On the other hand, the MHOFs with the stronger $\pi-\pi$ interaction L4 linker showed slower and smaller transformations to $NiOOH_{2-x}$ phases only at near-surface regions, where the MHOF can remain as a less active core. Further investigations are required to fully elucidate the origin of partial transformation in the L4-based MHOFs. One possibility is that it arises from the higher order of the linkers in the core of the MHOF particles, resulting in a strong adhesion force between linkers to remain metastable in base. This hypothesis is supported by observations that linker-related defects, such as dislocations, rotations, and kinks could be observed on the surface of the pristine MHOF particles.

Our detailed characterization thereby identifies MHOF as precatalysts to the more OER active $NiOOH_{2-x}$, but at the same time highlights the potential of stabilizing these MHOF materials under harsh and oxidizing conditions. Thus, targeted engineering to increase the $\pi-\pi$ stacking energy of the linkers, through methods such as functionalization or optimization of synthesis conditions to decrease defects, is promising for engineering stable structures inspired from those found in biological systems. Furthermore, since stable linkers prevent metal ion redox, which is a prerequisite for efficient OER, stabilizing the MHOF structure while promoting reversible redox processes is key toward enabling MHOFs as electrocatalysts for alkaline water oxidation. Therefore, future research efforts of stabilizing MHOFs as OER electrocatalysts should aim at not only achieving a stable structure but also promoting reversible cationic redox. Given the wide penetration of MOF materials within electrocatalysis and the poorly understood stability of these materials, our study provides extensive and direct insight paramount for the challenges and future design of OER active, yet stable MOFs.

ASSOCIATED CONTENT

Supporting Information

The Supporting Information is available free of charge at https://pubs.acs.org/doi/10.1021/acs.chemmater.3c00316.

Experimental methods: synthesis, electrochemical methods and protocols, electrolyte purification, elemental analysis, scanning electron microscopy, XPS, Raman spectroscopy, and preparation of SERS-active Au; calculation of TOF_{redox}; EXAFS fitting procedures including linear combination fitting (LCF); PXRD patterns, electrochemical characterization, Tafel plots, chronopotentiometric measurements, ADF and iDPC-STEM, EELS, XPS, SEM-EDX, EXAFS and structural parameters, SERS UV−vis spectroscopy proposed phase conversion of MHOFs in base (PDF)

AUTHOR INFORMATION

Corresponding Authors

Yuriy Román-Leshkov − *Department of Chemical Engineering, Massachusetts Institute of Technology, Cambridge, Massachusetts 02139, United States;* orcid.org/0000-0002-0025-4233; Email: yroman@mit.edu

Yang Shao-Horn − *Department of Materials Science and Engineering, Massachusetts Institute of Technology, Cambridge, Massachusetts 02139, United States; Research Laboratory of Electronics and Department of Mechanical Engineering, Massachusetts Institute of Technology, Cambridge, Massachusetts 02139, United States;* orcid.org/0000-0001-8714-2121; Email: shaohorn@mit.edu

Authors

Daniel J. Zheng − *Department of Materials Science and Engineering, Massachusetts Institute of Technology, Cambridge, Massachusetts 02139, United States;* orcid.org/0000-0002-9471-6856

Mikaela Görlin − *Research Laboratory of Electronics, Massachusetts Institute of Technology, Cambridge, Massachusetts 02139, United States; Department of Chemistry-Ångström Laboratory, Uppsala University, SE-75121 Uppsala, Sweden;* orcid.org/0000-0003-4472-955X

Kaylee McCormack − *Department of Chemical Engineering, Massachusetts Institute of Technology, Cambridge, Massachusetts 02139, United States*

Junghwa Kim − *Research Laboratory of Electronics, Massachusetts Institute of Technology, Cambridge, Massachusetts 02139, United States*

Jiayu Peng − *Department of Materials Science and Engineering, Massachusetts Institute of Technology, Cambridge, Massachusetts 02139, United States;* orcid.org/0000-0003-3696-770X

Hongbin Xu − *Department of Materials Science and Engineering, Massachusetts Institute of Technology, Cambridge, Massachusetts 02139, United States*

Xiaoxin Ma − *Chair of Inorganic and Metal−Organic Chemistry, Department of Chemistry & Catalysis Research Center, Technical University of Munich, 85748 Garching, Germany*

James M. LeBeau − *Department of Materials Science and Engineering, Massachusetts Institute of Technology, Cambridge, Massachusetts 02139, United States;* orcid.org/0000-0002-7726-3533

Roland A. Fischer − *Chair of Inorganic and Metal−Organic Chemistry, Department of Chemistry & Catalysis Research Center, Technical University of Munich, 85748 Garching, Germany;* orcid.org/0000-0002-7532-5286

Complete contact information is available at:

https://pubs.acs.org/10.1021/acs.chemmater.3c00316

Author Contributions

[▽]D.J.Z., M.G. contributed equally to this work. Y.S.-H, Y.R.-L., D.J.Z., and M.G. conceived the original study with assistance from K.M., D.J.Z. performed the synthesis and materials characterization with assistance from H.X. and K.M., D.J.Z. performed the electrochemical measurements and data analysis. D.J.Z. and M.G. performed the KOH electrolyte purification and ICP-MS elemental analysis. M.G. performed the operando SERS, UV−vis spectroscopy, SEM-EDX measurements, data analysis, and mechanistic considerations. J.K. performed the STEM and EELS measurements with analysis assistance from D.J.Z., K.M. performed the XPS and XAS measurements with analysis assistance from M.G., D.J.Z., M.G., K.M., Y.S.-H., and Y.R.-L. drafted the manuscript. All authors contributed to the revision of the manuscript.

Notes

The authors declare no competing financial interest.

■ ACKNOWLEDGMENTS

This work was supported by the Toyota Research Institute through the Accelerated Materials Design and Discovery program. M.G. acknowledges financial support from the Sweden-America Foundation, the Royal Swedish Academy of Engineering Sciences (IVA) via the Hans Werthén fund, and the Foundation Blanceflor Boncompagni Ludovisi, née Bildt. M.G. thanks the strategic research network StandUp for Energy. X.M. acknowledges the financial support from the China Scholarship Council. This work was carried out in part through the use of MIT.nano's facilities. Use of the Stanford Synchrotron Radiation Light source, SLAC National Accelerator Laboratory, is supported by the U.S. Department of Energy, Office of Science, Office of Basic Energy Sciences under Contract No. DE-AC02-76SF00515. Co-ACCESS is supported by the U.S. Department of Energy, Office of Basic Energy Sciences, Chemical Sciences, Geosciences and Biosciences Division. The authors thank Dr. Simon R. Bare, Dr. Adam S. Hoffman, and Dr. Jorge Perez-Aguilar (SLAC) for assisting with the XAS measurements and analysis.

■ REFERENCES

(1) Gray, H. B. Powering the Planet with Solar Fuel. *Nat. Chem.* **2009**, *1*, 7.
(2) Lee, Y.; Suntivich, J.; May, K. J.; Perry, E. E.; Shao-Horn, Y. Synthesis and Activities of Rutile IrO2 and RuO2 Nanoparticles for Oxygen Evolution in Acid and Alkaline Solutions. *J. Phys. Chem. Lett.* **2012**, *3*, 399−404.
(3) Wei, C.; Rao, R. R.; Peng, J.; Huang, B.; Stephens, I. E. L.; Risch, M.; Xu, Z. J.; Shao-Horn, Y. Recommended Practices and Benchmark Activity for Hydrogen and Oxygen Electrocatalysis in Water Splitting and Fuel Cells. *Adv. Mater.* **2019**, *31*, No. 1806296.
(4) David, M.; Ocampo-Martínez, C.; Sánchez-Peña, R. Advances in Alkaline Water Electrolyzers: A Review. *J. Energy Storage* **2019**, *23*, 392−403.
(5) Kuznetsov, D. A.; Han, B.; Yu, Y.; Rao, R. R.; Hwang, J.; Román-Leshkov, Y.; Shao-Horn, Y. Tuning Redox Transitions via Inductive Effect in Metal Oxides and Complexes, and Implications in Oxygen Electrocatalysis. *Joule* **2018**, *2*, 225−244.
(6) Zhou, H. C.; Long, J. R.; Yaghi, O. M. Introduction to Metal-Organic Frameworks. *Chem. Rev.* **2012**, *112*, 673−674.
(7) James, S. L. Metal-Organic Frameworks. *Chem. Soc. Rev.* **2003**, *32*, 276−288.
(8) Mukherjee, S.; Hou, S.; Watzele, S. A.; Garlyyev, B.; Li, W.; Bandarenka, A. S.; Fischer, R. A. Avoiding Pyrolysis and Calcination: Advances in the Benign Routes Leading to MOF-Derived Electrocatalysts. *ChemElectroChem* **2022**, *9*, No. e202101476.
(9) Liu, T.; Li, P.; Yao, N.; Cheng, G.; Chen, S.; Luo, W.; Yin, Y. CoP-Doped MOF-Based Electrocatalyst for PH-Universal Hydrogen Evolution Reaction. *Angew. Chem.* **2019**, *131*, 4727−4732.
(10) Fu, S.; Zhu, C.; Song, J.; Du, D.; Lin, Y. Metal-Organic Framework-Derived Non-Precious Metal Nanocatalysts for Oxygen Reduction Reaction. *Adv. Energy Mater.* **2017**, *7*, No. 1700363.
(11) Lu, X. F.; Xia, B. Y.; Zang, S.-Q.; Lou, X. W. David Metal−Organic Frameworks Based Electrocatalysts for the Oxygen Reduction Reaction. *Angew. Chem.* **2020**, *132*, 4662−4678.
(12) Zhao, S.; Wang, Y.; Dong, J.; He, C. T.; Yin, H.; An, P.; Zhao, K.; Zhang, X.; Gao, C.; Zhang, L.; Lv, J.; Wang, J.; Zhang, J.; Khattak, A. M.; Khan, N. A.; Wei, Z.; Zhang, J.; Liu, S.; Zhao, H.; Tang, Z. Ultrathin Metal-Organic Framework Nanosheets for Electrocatalytic Oxygen Evolution. *Nat. Energy* **2016**, *1*, No. 16184.
(13) Taffa, D. H.; Balkenhohl, D.; Amiri, M.; Wark, M. Minireview: Ni−Fe and Ni−Co Metal−Organic Frameworks for Electrocatalytic Water-Splitting Reactions. *Small Struct.* **2022**, *4*, No. 2200263.
(14) Linke, J.; Rohrbach, T.; Ranocchiari, M.; Schmidt, T. J.; Fabbri, E. Enlightening the Journey of Metal-Organic Framework (Derived) Catalysts during the Oxygen Evolution Reaction in Alkaline Media via Operando X-Ray Absorption Spectroscopy. *Curr. Opin. Electrochem.* **2021**, *30*, No. 100845.
(15) Zheng, W.; Lee, L. Y. S. Metal-Organic Frameworks for Electrocatalysis: Catalyst or Precatalyst? *ACS Energy Lett.* **2021**, *6*, 2838−2843.
(16) Li, W.; Watzele, S.; El-Sayed, H. A.; Liang, Y.; Kieslich, G.; Bandarenka, A. S.; Rodewald, K.; Rieger, B.; Fischer, R. A. Unprecedented High Oxygen Evolution Activity of Electrocatalysts Derived from Surface-Mounted Metal-Organic Frameworks. *J. Am. Chem. Soc.* **2019**, *141*, 5926−5933.
(17) Zheng, W.; Liu, M.; Lee, L. Y. S. Electrochemical Instability of Metal-Organic Frameworks: In Situ Spectroelectrochemical Investigation of the Real Active Sites. *ACS Catal.* **2020**, *10*, 81−92.
(18) Zhao, S.; Tan, C.; He, C. T.; An, P.; Xie, F.; Jiang, S.; Zhu, Y.; Wu, K. H.; Zhang, B.; Li, H.; Zhang, J.; Chen, Y.; Liu, S.; Dong, J.; Tang, Z. Structural Transformation of Highly Active Metal−Organic Framework Electrocatalysts during the Oxygen Evolution Reaction. *Nat. Energy* **2020**, *5*, 881−890.
(19) Yuan, S.; Peng, J.; Cai, B.; Huang, Z.; Garcia-Esparza, A. T.; Sokaras, D.; Zhang, Y.; Giordano, L.; Akkiraju, K.; Zhu, Y. G.; Hübner, R.; Zou, X.; Román-Leshkov, Y.; Shao-Horn, Y. Tunable Metal Hydroxide−Organic Frameworks for Catalysing Oxygen Evolution. *Nat. Mater.* **2022**, *21*, 673−680.
(20) Ma, X.; Zheng, D. J.; H; Mukherjee, S.; Khare, R.; Gao, G.; Ai, Q.; Garlyyev, B.; Li, W.; Koch, M.; Mink, J.; Shao-Horn, Y.; Warnan, J.; Bandarenka, A. S.; Fischer, R. Structure-Activity Relationships in Ni- Carboxylate-Type Metal-Organic Frameworks' Metamorphosis for Oxygen Evolution Reaction. *ACS Catal.* **2023**, *12*, 7587−7596.
(21) Dionigi, F.; Strasser, P. NiFe-Based (Oxy)Hydroxide Catalysts for Oxygen Evolution Reaction in Non-Acidic Electrolytes. *Adv. Energy Mater.* **2016**, *6*, No. 1600621.
(22) Goldsmith, Z. K.; Harshan, A. K.; Gerken, J. B.; Voros, M.; Galli, G.; Stahl, S. S.; Hammes-Schiffer, S. Characterization of NiFe Oxyhydroxide Electrocatalysts by Integrated Electronic Structure Calculations and Spectroelectrochemistry. *Proc. Natl. Acad. Sci. U.S.A.* **2017**, *114*, 3050−3055.
(23) Trotochaud, L.; Young, S. L.; Ranney, J. K.; Boettcher, S. W. Nickel-Iron Oxyhydroxide Oxygen-Evolution Electrocatalysts: The Role of Intentional and Incidental Iron Incorporation. *J. Am. Chem. Soc.* **2014**, *136*, 6744−6753.
(24) Diaz-Morales, O.; Ferrus-Suspedra, D.; Koper, M. T. M. The Importance of Nickel Oxyhydroxide Deprotonation on Its Activity towards Electrochemical Water Oxidation. *Chem. Sci.* **2016**, *7*, 2639−2645.

(25) Moysiadou, A.; Lee, S.; Hsu, C. S.; Chen, H. M.; Hu, X. Mechanism of Oxygen Evolution Catalyzed by Cobalt Oxyhydroxide: Cobalt Superoxide Species as a Key Intermediate and Dioxygen Release as a Rate-Determining Step. *J. Am. Chem. Soc.* **2020**, *142*, 11901−11914.
(26) Yeo, B. S.; Bell, A. T. In Situ Raman Study of Nickel Oxide and Gold-Supported Nickel Oxide Catalysts for the Electrochemical Evolution of Oxygen. *J. Phys. Chem. C* **2012**, *116*, 8394−8400.
(27) Görlin, M.; De Araujo, J. F.; Schmies, H.; Bernsmeier, D.; Dresp, S.; Gliech, M.; Jusys, Z.; Chernev, P.; Kraehnert, R.; Dau, H.; Strasser, P. Tracking Catalyst Redox States and Reaction Dynamics in Ni-Fe Oxyhydroxide Oxygen Evolution Reaction Electrocatalysts: The Role of Catalyst Support and Electrolyte pH. *J. Am. Chem. Soc.* **2017**, *139*, 2070−2082.
(28) Stevens, M. B.; Trang, C. D. M.; Enman, L. J.; Deng, J.; Boettcher, S. W. Reactive Fe-Sites in Ni/Fe (Oxy)Hydroxide Are Responsible for Exceptional Oxygen Electrocatalysis Activity. *J. Am. Chem. Soc.* **2017**, *139*, 11361−11364.
(29) Louie, M. W.; Bell, A. T. An Investigation of Thin-Film Ni-Fe Oxide Catalysts for the Electrochemical Evolution of Oxygen. *J. Am. Chem. Soc.* **2013**, *135*, 12329−12337.
(30) Barnard, R.; Randell, C. F.; Tye, F. L. Studies Concerning Charged Nickel Hydroxide Electrodes I. Measurement of Reversible Potentials. *J. Appl. Electrochem.* **1980**, *10*, 109−125.
(31) Fu, X. Z.; Zhu, Y. J.; Xu, Q. C.; Li, J.; Pan, J. H.; Xu, J. Q.; Lin, J. D.; Liao, D. W. Nickel Oxyhydroxides with Various Oxidation States Prepared by Chemical Oxidation of Spherical β-Ni(OH)2. *Solid State Ionics* **2007**, *178*, 987−993.
(32) Doyle, R. L.; Godwin, I. J.; Brandon, M. P.; Lyons, M. E. G. Redox and Electrochemical Water Splitting Catalytic Properties of Hydrated Metal Oxide Modified Electrodes. *Phys. Chem. Chem. Phys.* **2013**, *15*, 13737−13783.
(33) Roy, C.; Sebok, B.; Scott, S. B.; Fiordaliso, E. M.; Sørensen, J. E.; Bodin, A.; Trimarco, D. B.; Damsgaard, C. D.; Vesborg, P. C. K.; Hansen, O.; Stephens, I. E. L.; Kibsgaard, J.; Chorkendorff, I. Impact of Nanoparticle Size and Lattice Oxygen on Water Oxidation on NiFeOxHy. *Nat. Catal.* **2018**, *1*, 820−829.
(34) Lee, S.; Banjac, K.; Lingenfelder, M.; Hu, X. Oxygen Isotope Labeling Experiments Reveal Different Reaction Sites for the Oxygen Evolution Reaction on Nickel and Nickel Iron Oxides. *Angew. Chem., Int. Ed.* **2019**, *58*, 10295−10299.
(35) Ferreira de Araújo, J.; Dionigi, F.; Merzdorf, T.; Oh, H. S.; Strasser, P. Evidence of Mars-Van-Krevelen Mechanism in the Electrochemical Oxygen Evolution on Ni-Based Catalysts. *Angew. Chem., Int. Ed.* **2021**, *60*, 14981−14988.
(36) Hou, S.; Li, W.; Watzele, S.; Kluge, R. M.; Xue, S.; Yin, S.; Jiang, X.; Döblinger, M.; Welle, A.; Garlyyev, B.; Koch, M.; Müller-Buschbaum, P.; Wöll, C.; Bandarenka, A. S.; Fischer, R. A. Metamorphosis of Heterostructured Surface-Mounted Metal−Organic Frameworks Yielding Record Oxygen Evolution Mass Activities. *Adv. Mater.* **2021**, *33*, No. 2103218.
(37) Görlin, M.; Chernev, P.; De Araújo, J. F.; Reier, T.; Dresp, S.; Paul, B.; Krähnert, R.; Dau, H.; Strasser, P. Oxygen Evolution Reaction Dynamics, Faradaic Charge Efficiency, and the Active Metal Redox States of Ni-Fe Oxide Water Splitting Electrocatalysts. *J. Am. Chem. Soc.* **2016**, *138*, 5603−5614.
(38) Hall, D. S.; Lockwood, D. J.; Bock, C.; MacDougall, B. R. Nickel Hydroxides and Related Materials: A Review of Their Structures, Synthesis and Properties. *Proc. R. Soc. A* **2015**, *471*, No. 20140792.
(39) Hall, D. S.; Bock, C.; MacDougall, B. R. The Electrochemistry of Metallic Nickel: Oxides, Hydroxides, Hydrides and Alkaline Hydrogen Evolution. *J. Electrochem. Soc.* **2013**, *160*, F235−F243.
(40) Biesinger, M. C.; Payne, B. P.; Grosvenor, A. P.; Lau, L. W. M.; Gerson, A. R.; Smart, R. S. C. Resolving Surface Chemical States in XPS Analysis of First Row Transition Metals, Oxides and Hydroxides: Cr, Mn, Fe, Co and Ni. *Appl. Surf. Sci.* **2011**, *257*, 2717−2730.
(41) Ali-Löytty, H.; Louie, M. W.; Singh, M. R.; Li, L.; Sanchez Casalongue, H. G.; Ogasawara, H.; Crumlin, E. J.; Liu, Z.; Bell, A. T.; Nilsson, A.; Friebel, D. Ambient-Pressure XPS Study of a Ni-Fe Electrocatalyst for the Oxygen Evolution Reaction. *J. Phys. Chem. C* **2016**, *120*, 2247−2253.
(42) Arai, H.; Tsuda, M.; Saito, K.; Hayashi, M.; Takei, K.; Sakurai, Y. Structural and Thermal Characteristics of Nickel Dioxide Derived from LiNiO2. *J. Solid State Chem.* **2002**, *163*, 340−349.
(43) Kovács, G.; Bertóti, I.; Radnóczi, G. X-Ray Photoelectron Spectroscopic Study of Magnetron Sputtered Carbon−Nickel Composite Films. *Thin Solid Films* **2008**, *516*, 7942−7946.
(44) Ulrich, S.; Jung, U.; Strunskus, T.; Schütt, C.; Bloedorn, A.; Lemke, S.; Ludwig, E.; Kipp, L.; Faupel, F.; Magnussen, O.; Herges, R. X-Ray Spectroscopy Characterization of Azobenzene-Functionalized Triazatriangulenium Adlayers on Au(111) Surfaces. *Phys. Chem. Chem. Phys.* **2015**, *17*, 17053−17062.
(45) Qian, Q.; Li, Y.; Liu, Y.; Yu, L.; Zhang, G. Ambient Fast Synthesis and Active Sites Deciphering of Hierarchical Foam-Like Trimetal−Organic Framework Nanostructures as a Platform for Highly Efficient Oxygen Evolution Electrocatalysis. *Adv. Mater.* **2019**, *31*, No. 1901139.
(46) Mousazade, Y.; Mohammadi, M. R.; Chernev, P.; Bagheri, R.; Song, Z.; Dau, H.; Najafpour, M. M. Revisiting Metal−Organic Frameworks for Oxygen Evolution: A Case Study. *Inorg. Chem.* **2020**, *59*, 15335−15342.
(47) Zhu, Y.; Cao, C.; Tao, S.; Chu, W.; Wu, Z.; Li, Y. Ultrathin Nickel Hydroxide and Oxide Nanosheets: Synthesis, Characterizations and Excellent Supercapacitor Performances. *Sci. Rep.* **2014**, *4*, No. 5787.
(48) Trześniewski, B. J.; Diaz-Morales, O.; Vermaas, D. A.; Longo, A.; Bras, W.; Koper, M. T. M.; Smith, W. A. In Situ Observation of Active Oxygen Species in Fe-Containing Ni-Based Oxygen Evolution Catalysts: The Effect of PH on Electrochemical Activity. *J. Am. Chem. Soc.* **2015**, *137*, 15112−15121.
(49) Lee, S.; Bai, L.; Hu, X. Deciphering Iron-Dependent Activity in Oxygen Evolution Catalyzed by Nickel−Iron Layered Double Hydroxide. *Angew. Chem., Int. Ed.* **2020**, *59*, 8072−8077.
(50) Merrill, M.; Worsley, M.; Wittstock, A.; Biener, J.; Stadermann, M. Determination of the "NiOOH" Charge and Discharge Mechanisms at Ideal Activity. *J. Electroanal. Chem.* **2014**, *717*−*718*, 177−188.
(51) Qiu, Z.; Ma, Y.; Edvinsson, T. In Operando Raman Investigation of Fe Doping Influence on Catalytic NiO Intermediates for Enhanced Overall Water Splitting. *Nano Energy* **2019**, *66*, No. 104118.
(52) Liu, X.; Xia, F.; Guo, R.; Huang, M.; Meng, J.; Wu, J.; Mai, L. Ligand and Anion Co-Leaching Induced Complete Reconstruction of Polyoxomolybdate-Organic Complex Oxygen-Evolving Pre-Catalysts. *Adv. Funct. Mater.* **2021**, *31*, No. 2101792.
(53) Kostecki, R.; McLarnon, F. Electrochemical and In Situ Raman Spectroscopic Characterization of Nickel Hydroxide Electrodes: I. Pure Nickel Hydroxide. *J. Electrochem. Soc.* **1997**, *144*, 485−493.
(54) Klaus, S.; Cai, Y.; Louie, M. W.; Trotochaud, L.; Bell, A. T. Effects of Fe Electrolyte Impurities on Ni(OH)2/NiOOH Structure and Oxygen Evolution Activity. *J. Phys. Chem. C* **2015**, *119*, 7243−7254.
(55) Friebel, D.; Louie, M. W.; Bajdich, M.; Sanwald, K. E.; Cai, Y.; Wise, A. M.; Cheng, M. J.; Sokaras, D.; Weng, T. C.; Alonso-Mori, R.; Davis, R. C.; Bargar, J. R.; Nørskov, J. K.; Nilsson, A.; Bell, A. T. Identification of Highly Active Fe Sites in (Ni,Fe)OOH for Electrocatalytic Water Splitting. *J. Am. Chem. Soc.* **2015**, *137*, 1305−1313.
(56) Rao, R. R.; Corby, S.; Bucci, A.; García-Tecedor, M.; Mesa, C. A.; Rossmeisl, J.; Giménez, S.; Lloret-Fillol, J.; Stephens, I. E. L.; Durrant, J. R. Spectroelectrochemical Analysis of the Water Oxidation Mechanism on Doped Nickel Oxides. *J. Am. Chem. Soc.* **2022**, *144*, 7622−7633.
(57) Francàs, L.; Corby, S.; Selim, S.; Lee, D.; Mesa, C. A.; Godin, R.; Pastor, E.; Stephens, I. E. L.; Choi, K.-S.; Durrant, J. R. Spectroelectrochemical Study of Water Oxidation on Nickel and Iron Oxyhydroxide Electrocatalysts. *Nat. Commun.* **2019**, *10*, No. 5208.

https://doi.org/10.1021/acs.chemmater.3c00316
Chem. Mater. XXXX, XXX, XXX−XXX

(58) Xiao, Z.; Mei, Y.; Yuan, S.; Mei, H.; Xu, B.; Bao, Y.; Fan, L.; Kang, W.; Dai, F.; Wang, R.; Wang, L.; Hu, S.; Sun, D.; Zhou, H.-C. Controlled Hydrolysis of Metal−Organic Frameworks: Hierarchical Ni/Co-Layered Double Hydroxide Microspheres for High-Performance Supercapacitors. *ACS Nano* **2019**, *13*, 7024−7030.
(59) Burtch, N. C.; Jasuja, H.; Walton, K. S. Water Stability and Adsorption in Metal−Organic Frameworks. *Chem. Rev.* **2014**, *114*, 10575−10612.
(60) Ni, C.; Zheng, H.; Liu, W.; Wu, L.; Li, R.; Zhou, K.; Zhang, W. Linker Defects in Metal−Organic Frameworks for the Construction of Interfacial Dual Metal Sites with High Oxygen Evolution Activity. *Adv. Funct. Mater.* **2023**, *33*, 2301075.
(61) Xiang, W.; Zhang, Y.; Chen, Y.; Liu, C.; Tu, X. Synthesis, Characterization and Application of Defective Metal−Organic Frameworks: Current Status and Perspectives. *J. Mater. Chem. A* **2020**, *8*, 21526−21546.
(62) Li, N.; Bediako, D. K.; Hadt, R. G.; Hayes, D.; Kempa, T. J.; Von Cube, F.; Bell, D. C.; Chen, L. X.; Nocera, D. G. Influence of Iron Doping on Tetravalent Nickel Content in Catalytic Oxygen Evolving Films. *Proc. Natl. Acad. Sci. U.S.A.* **2017**, *114*, 1486−1491.

https://doi.org/10.1021/acs.chemmater.3c00316
Chem. Mater. XXXX, XXX, XXX−XXX